THERMAL ANALYSIS OF DIRECTIONAL DRILLING TOOL IN HIGH HEAT FLUX ENVIRONMENT

by

Kenichiro Jin

SUBMITTED TO THE DEPARTMENT OF MECHANICAL ENGINEERING
IN PARTIAL FULFILLMENT OF THE REQUIREMENTS FOR THE DEGREES OF

BACHELOR OF SCIENCE

AND

MASTER OF SCIENCE

AT THE
MASSACHUSETTS INSTITUTE OF TECHNOLOGY
June 2002

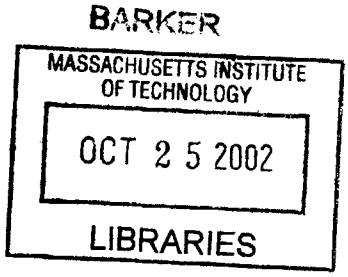

Signature of Author:___ _____
Department of Mechanical Engineering
May 10, 2002

Certified by:_____
John H. Lienhard V
Professor of Mechanical Engineering
Thesis Supervisor

Accepted by:_____
Ain A. Sonin
Chairman, Department Committee on Graduate Students

THERMAL ANALYSIS OF DIRECTIONAL DRILLING TOOL IN HIGH HEAT FLUX ENVIRONMENT

by

Kenichiro Jin

Submitted to the Department of Mechanical Engineering
on May 10, 2002 in Partial Fulfillment of the
Requirements for the Degrees of Bachelor of Science
and Master of Science

ABSTRACT

A thermal analysis was performed on the steering section of Schlumberger's Direct675 Counter Rotary Steerable Directional Drilling tool. This analysis will compensate for the lack of a test procedure for analyzing the thermal state of the tool during the design process. The steering section of this tool is known to generate high heat fluxes, which are cooled by the internal and annular drilling mud flow whose flow rate ranges from 40 ft/s to 80 ft/s. However, the drilling mud itself can reach temperatures of up to 175°C. The surrounding environment also reaches temperatures of up to 200°C whose heat flux is also absorbed by the drilling mud flow. The aforementioned factors all influence the heat dissipation within the tool and can be a cause of dangerous "hot spots" that may cause system failures, which leads to lost drilling time and a decrease in cost efficiency.

The drilling mud flow analysis showed that the environmental heat flux does not have a significant affect on the overall heat dissipation of the tool. Both the temperature gradient in the mud and the temperature differentials across the cross section of the tool were insignificantly changed with the influence of environmental heat flux. The finite difference analysis results showed an accurate representation of the temperature distribution within the motor section. This analysis showed that under a worst-case scenario, the maximum temperature reached 253.089°C within the motor section. In analyzing the temperature differential across the cross section of the section, several layers indicated inefficient heat dissipation which may lead to electrical meltdowns. In utilizing all the information obtained from the thermal analysis, the maximum temperatures can be decreased with the change of several design factors.

Thesis Supervisor: John H. Lienhard V
Title: Professor of Mechanical Engineering

TABLE OF CONTENTS

LIST OF FIGURES

CHAPTER 4

APPENDIX A

APPENDIX B

LIST OF TABLES

CHAPTER 1

PROJECT BACKGROUND - ADVANCED DRILLING TECHNOLOGIES

Although it is estimated that only one-third of the world's oil reservoirs have been tapped, they have been become harder to locate and, in many instances, very difficult using existing technologies to reach due to their physical locations. However, the advent of advanced drilling technologies, specifically directional drilling, has revolutionized the drilling industry.

Many situations require directional drilling technologies. Standard drilling technologies are often limited by geological characteristics. Inaccessible reservoir locations may require complicated well trajectories to reach wells that include horizontal and extended reach wells. Salt domes often create hydrocarbon traps where the reservoir is located directly beneath its edge. Because drilling through salt domes may causes problems such as severe washouts and salt flows, a directional well can be used to avoid the salt dome and to reach the reservoir. When a fault is located in close proximity to a reservoir, fault slippage may cause casing damage if a well were to be drilled through it. This can be avoided by drilling parallel to the fault, no matter the orientation, to reach the reservoir.

Production issues have also contributed to the success of directional drilling. Drilling multilateral wells has been a standard offshore practice for many years due to the

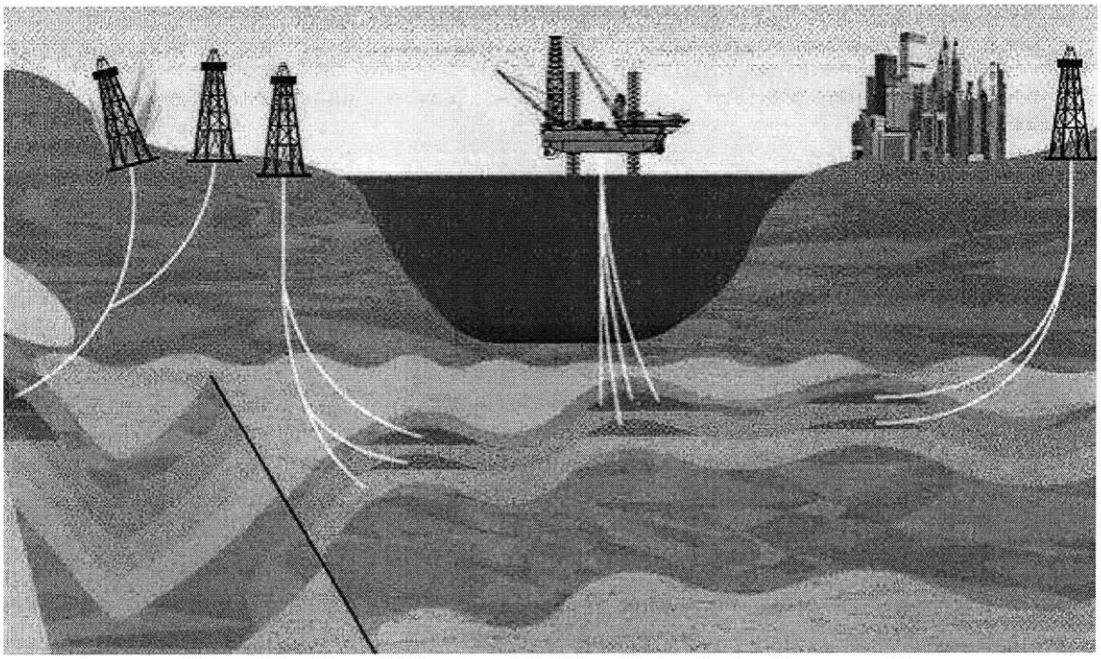

Figure 1.1. Uses of Directional Drilling Technologies, Downton [1]

limitations set on building oil rigs. Now, drilling multiple wells is commonly used in onshore locations because it allows for the drainage of several reservoir compartments located in one field. Small compartments discovered in mature fields can also be reached with well-located wells created utilizing directional drilling. Horizontal well drilling has proven to increase the accessibility to formations, which helps to increase flow and production.

In emergency oilfield situations, the use of a directional drilling system is often unavoidable. An example of such a situation is the process of drilling relief wells for blowouts. Blow-outs can cause damage or destruction to the rigs. A relief well can be drilled to control the blown well as well as to continue producing from the existing reservoir. These types of uses for directional drilling technologies are illustrated in Figure 1.1.

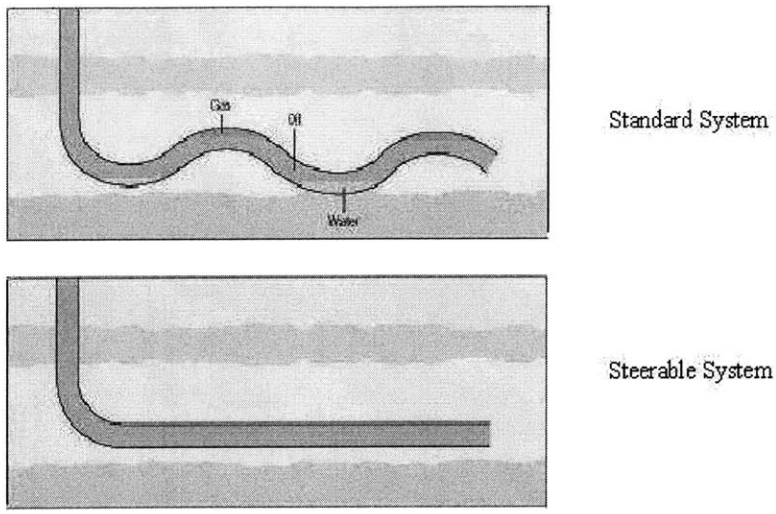

Figure 1.2. Advantage of Directional Drilling in Straight Hole Drilling, Downton [1]

Directional drilling technologies can also help in the control of drilling processes. Certain drilling conditions may cause standards drills to follow an erratic path. However, with a steerable drilling system, changing the orientation of the drill bit can help to control the well trajectory and straighten the well as shown in Figure 1.2. Sidetracking control is also used when obstructions, such as stuck drill pipes, occur in well bores.

Schlumberger is a leader in the oilfield service industry, providing services ranging from seismic surveys, drilling, wireline logging, well construction, and completion. As a leader in the industry, they develop leading edge technologies for all oilfield services, including drilling systems. Specifically, Schlumberger has joined the drilling industry in developing technological advances with rotary steerable systems. A rotary steerable system allows for the continuous rotation of the drill string while steering the drill bit. This type of system increases the efficiency of the drilling process by minimizing such well bore effects as tortuosity, increased torque, and drag while still having the ability to orient the drill bit in the desired trajectory.

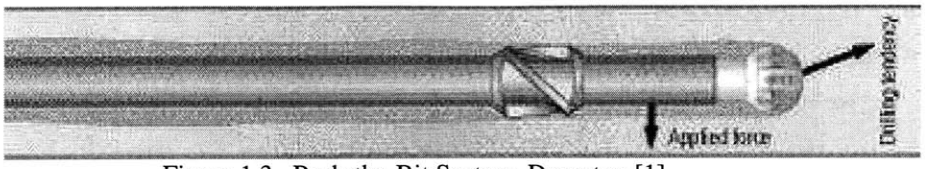

Figure 1.3. Push-the-Bit System, Downton [1]

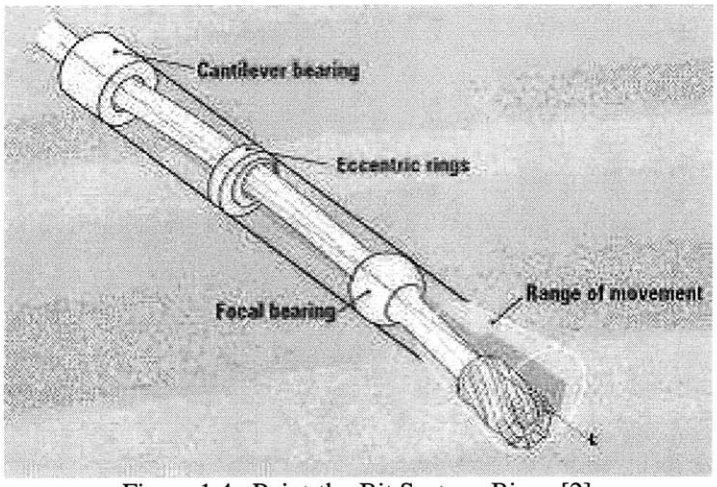

Figure 1.4. Point-the-Bit System, Biggs [2]

The PowerDrive Rotary Steerable Drilling System, which is in production by Schlumberger, has already proven itself as an effective directional drilling system in the field. This system is a "push-the-bit" system where the drilling direction is determined by an applied force to the well bore wall as shown in Figure 1.3. This system entails three actuator pads located behind the drill bit that is controlled by the internal mud flow with the use of a valve system. These actuators apply a force in a certain direction to obtain the desired bit trajectory.

The Advanced Drilling Group at Schlumberger has developed a new rotary steerable system, which is the next step in advanced drilling technologies – the Direct675 Counter Rotary Steerable Drilling System. The Direct675 system differs from the existing PowerDrive system in that this is a "point-the-bit" tool design where the drilling direction is determined by the trajectory of the drill bit as shown in Figure 1.4.

"Point-the-bit" systems go beyond the flow and temperature ranges of "push-the-bit" systems and further optimizes recovery and financial returns. This type of system can reduce cutting accumulation around the BHA (bottom-hole assembly), the likeliness of becoming stuck, and increase the ability to back ream the well bore.

1.1 Direct675 Counter Rotary System

The Direct675 Counter Rotary System consists of three main modules – the power generation module, the electronics module, and the steering section. The power generation module consists of a turbine and an alternator which is driven by the internal mud flow. This creates the power to drive the electronics and the motor. This type of power generation allows for longer runs compared to battery powered tools. The electronics module holds the electronic components of this tool that control the motor, which includes the sensors packages. The sensors monitor the rotation of the collar as well as the output shaft of the motor. These sensors also take direction and inclination measurements during drilling.

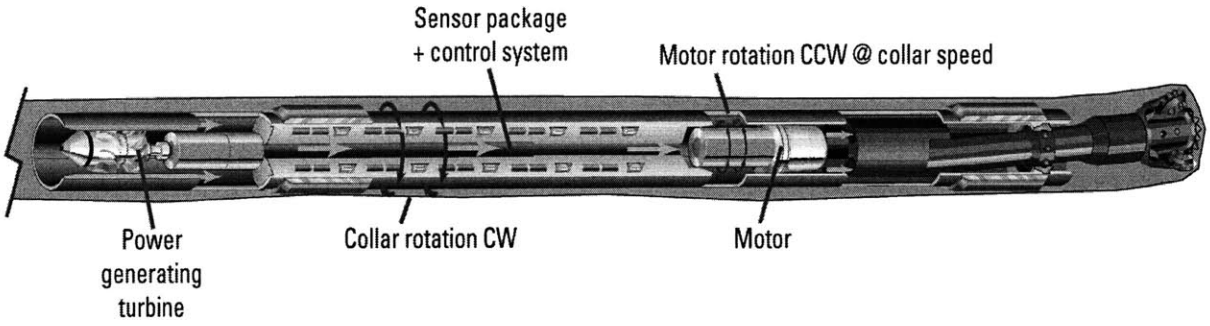

Figure 1.5. General description of Direct675 Counter Rotary System, Pafitis [3]

The steering section is the key module of this tool. Although all three modules generate a large amount of heat, the main focus of this analysis is the steering section. This module sets the trajectory of the drill bit, which determines the drilling direction.

The steering section can be divided into 5 main sub-assemblies – the motor, the gear box, the pressure compensator, the offset mandrel, and the bit shaft. The bit shaft contains a universal joint that absorbs thrust and torque as well as providing the offset of the tool which is controlled by the motor. This offset, which controls the direction of the bit, is maintained by an internal mandrel, which remains geo-stationary during collar rotation.

1.2 Drilling Economics

When first developed, rotary steerable systems were utilized in extended well drilling processes where traditional directional drilling systems were limited. However, due to the economic benefits of these systems, they have also been applied in recent years to wells that do not require their technical capabilities.

The discovery and development process in the oilfield industry may result in very high rewards but it also carries very high costs. Specifically, approximately 40% of the costs as well as the total development times are accounted for by drilling procedures as given by Dawe [4]. Figure 1.5 shows the breakdown of the cost distribution of an example field development process where the highlighted elements represent the costs due to drilling procedures and equipment. Figure 1.6 shows the time distribution for the same development process.

All the advantages associated with directional drilling technologies, such as increased production, reduced costs, and time efficiency, combine to help reach the ultimate goal in mainstream operations, which is to increase the cost effectiveness of the entire process.

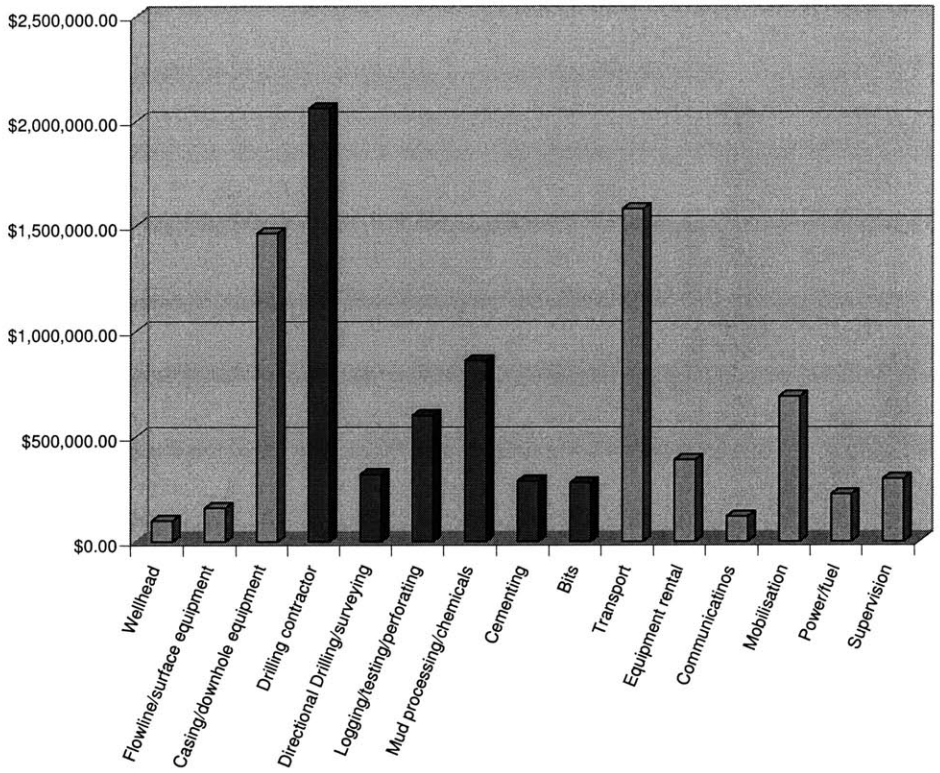

Figure 1.6. Cost Distribution of Field Development Process

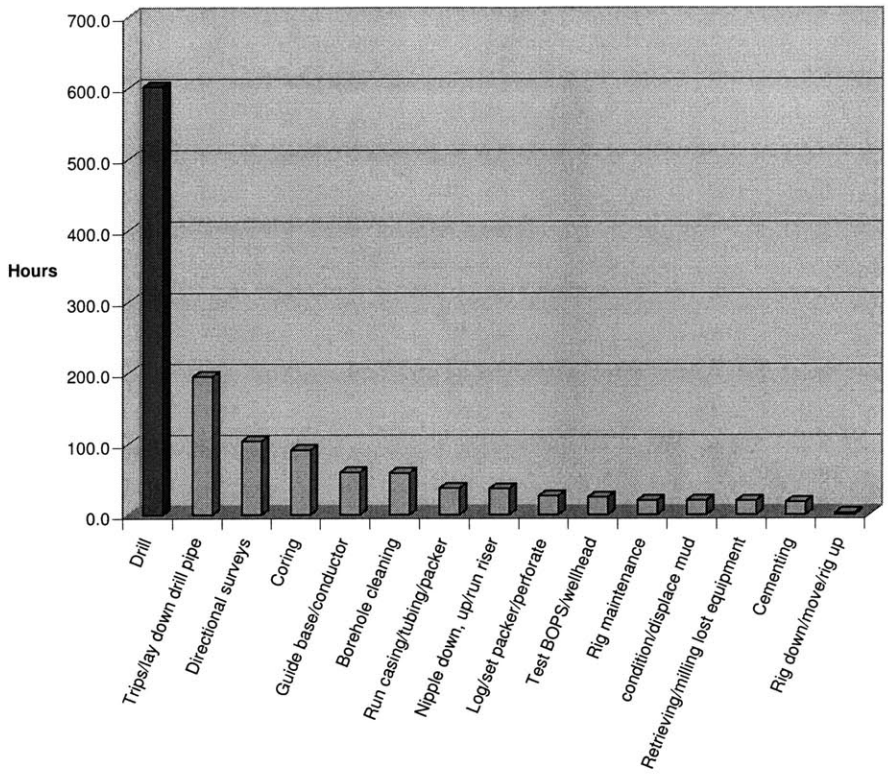

Figure 1.7. Time Distribution of Field Development Process

1.3 Motivation

Downhole tool breakdowns are a major cost factor in the drilling process. If a tool breaks, the recovery of the tool and lost drilling time can dramatically decrease the cost effectiveness of the process. While the technological advances of the Direct675 system can increase the cost effectiveness of the drilling process, malfunctions that lead to system failures can negate the benefits gained from the technology. One such scenario that is a possibility in all oilfield service equipment is a thermal break down within the tool. Oilfield service equipment operates at very high temperatures due the several factors such as high heat drilling mud flow, internal heat generation from tool components, and exposure to high heat flux environments. Internal mud flows can reach

up to 175°C. The surrounding environment can reach temperatures in the range of 200°C at any depth. The tools must be well-designed thermally to optimize heat dissipation or thermal breakdowns can result.

Due to the high temperatures and also the physical limitations of the drilling tools themselves, there currently exists no testing procedure to analyze the thermal state of the tool in its high heat flux environments. In the laboratory, the tool can be tested with a load to simulate the weight-on-bit. However, this does not take into account the affects of the mud flow or the environmental heat fluxes. Further analysis can be performed through field tests. Field testing procedures allows for testing of tools in down hole conditions. However, this testing procedure takes into place after a tool has been designed and prototyped. At this stage in the design process, inefficient thermal design may cause break downs and add to the cost of design. It may also delay product placement into the oilfield service markets. By ignoring the thermal state of the tool in high heat flux environments, many sacrifices will be made in terms of time, revenues, and profits.

The purpose of this thesis is to develop a theoretical thermal analysis of the Direct675 steering system whose assembly includes a brushless DC motor, planetary gearbox, and a universal joint that transmits torque and thrust. This analysis will focus on the effect of the drilling fluid of the tool, often referred to as drilling mud, on the heat fluxes generated by the system. The drilling mud acts as the coolant along both the internal and the annular flows of the tool. Furthermore, the analysis will be extended to determine the temperature distributions within the main mechanical components of the system in order to determine the existence of any internal "hot spots" that may lead to

tool failure. This identification of problem areas will lead to the evaluation of possible design changes to the tool to increase its reliability. The results of this model will allow designers to obtain a preliminary analysis of the thermal state of the system in high heat flux environments.

1.4 Initial Observations

In order to determine the main areas of focus on the steering section for the thermal analysis, the tool was examined in the laboratory. The test set-up consisted of only the electronics module and the motor section, powered and controlled by a laboratory control unit. With the use of a standard hydraulic test fixture, a load of 20kpsi was applied to the bit shaft of the steering section to simulate weight-on-bit during drilling. The tool was inspected with the actuator rotating at maximum speed from start-up to steady state.

First by physical inspection, the main areas within the steering section that generated noticeable heat flux in a room temperature environment were the areas surrounding the motor and the thrust rings, which is located in the bit shaft. All other sections did not display any noticeable heat flux.

In order to obtain a more accurate reading of heat generation, the tool was examined using an infrared thermal imaging camera. Thermal imaging devices give a visual representation of radiant energy emitted by objects. With the use of this camera, the visual and physical inspections were confirmed. While areas of the motor and the

thrust rings showed high temperature differentials, the other sections of the steering section showed little or no temperature differential.*

With the results obtained from both the physical inspection and the infrared thermal imaging, it was decided to focus on the motor and the thrust rings of the steering section as the main sources of heat flux generation.

* Note: Because a third party vendor was called in to conduct the infrared thermal imaging as a demonstration, no thermal images were obtained for the report.

CHAPTER 2

THERMAL ANALYSIS – ADIABATIC BORE HOLE

2.1 Heat Transfer Analysis of Drilling Mud Flow

Because of the difficulties of characterizing the non-Newtonian properties of drilling mud, its properties have been replaced with the properties of water. Because of the high flow rates, the mud flows are modeled as turbulent; hence, the hydrodynamic properties of a non-Newtonian fluid can be compared with those of a Newtonian fluid such as water. The composition of drilling mud is mainly water. Therefore substituting the thermodynamic properties of water will give approximate results for this model.

The pattern of the flow is described in Figure 2.1. The mud enters the steering section through the inner diameter of the tool and exits at the end of the bit shaft. At this point, the mud exits the inner diameter and begins to flow back up through the annulus. This flow is the main source of heat dissipation. The range of the flow rate has been defined to be between 40 ft/s to 80 ft/s in order to drive the tool.

Although heat is also generated at the bit surface, this energy will be ignored in this modeling.

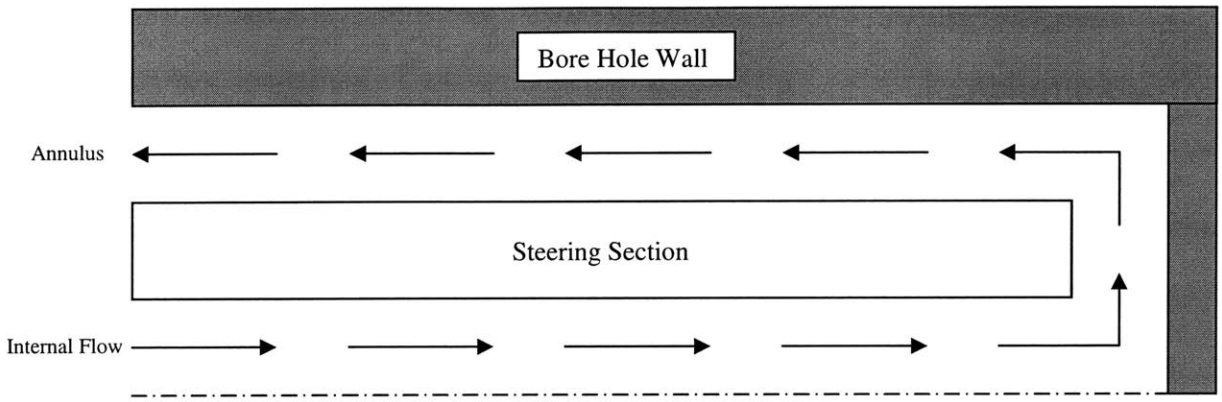

Figure 2.1. Path of Mud Flow through Tool and Annulus

2.1.1 Analysis of Internal Flow

The internal flow is modeled as fully developed because the steering section is situated at the end of the drill string. In order to determine the heat transfer coefficient of the internal flow through the flex tube, correlations for pipes were used.

In order to classify the flow as laminar or turbulent, the Reynolds number was determined:

$$\mathrm{Re}_D = \frac{4\dot{m}}{\pi D_{flex}\mu_{water}} \qquad 2.1$$

where D_{flex} is the diameter of the flex tube and μ_{water} is the viscosity of water. The mass flow rate, $\dot{m}$, was determined by:

$$\dot{m} = \rho_{water} A_{c,fl} v_{mud} \qquad 2.2$$

where ρ_{water} is the density of water, $A_{c,fl}$ is the cross sectional area of the flex tube, and v_{mud} is the velocity of the flow.

For flow rates between 40 ft/s to 80 ft/s, the Reynolds numbers were determined to be at turbulent levels ranging from 3440.85 to 6881.71, as shown in Figure 2.3.

Therefore, in order to determine the Nusselt number for this flow, the following relationship was used:

$$Nu_D = \frac{\frac{f}{8}(\mathrm{Re}_D - 1000)\mathrm{Pr}}{\left\{1 + \left[12.7\left(\frac{f}{8}\right)^{\frac{1}{2}}\left(\mathrm{Pr}^{\frac{2}{3}} - 1\right)\right]\right\}}. \qquad 2.3$$

The friction factor, f, is determined by:

$$f = [0.79\ln(\mathrm{Re}_D) - 1.64]^{-2} \qquad 2.4$$

and the Prandtl number, Pr, is determined by:

$$\mathrm{Pr} = \frac{c_{p,water}\mu_{water}}{k_{water}} \qquad 2.5$$

where $c_{p,water}$ is the specific heat of water, and k_{water} is the thermal conductivity of water.

Determining the Nusselt number gives the heat transfer coefficient of the internal flow in the flex tube as:

$$h_i = \frac{Nu_D k_{water}}{D_{flex}}. \qquad 2.6$$

Figure 2.2 gives the variation in the heat transfer coefficient of the internal flow with the flow rate. As Figure 2.2 indicates a transition from laminar to turbulent flow occurs at approximately 26 ft/s. For laminar flow, Incropera and DeWitt [5] define the Nusselt number is defined to be 3.66.

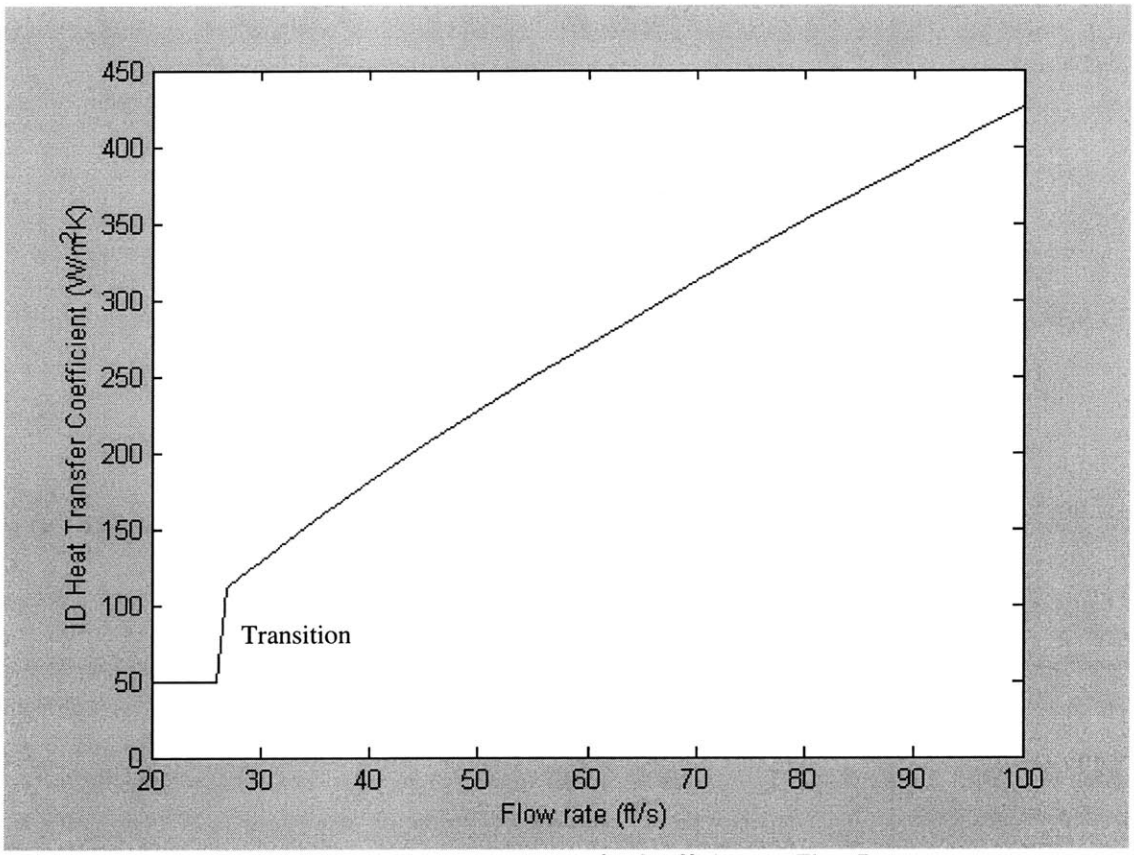

Figure 2.2. Internal Heat Transfer Coefficient vs. Flow Rate

2.1.2 Analysis of Annulus Flow

The annular flow is a result of the mud flow exiting the flex tube in the downward direction and entering the annulus in the upward direction. Therefore, it is not feasible to model this flow as fully developed as in the previous section for the internal flow. This section will compare two different annular flow models to determine the best estimate for this system.

Before considering the models, the Reynolds number for the annulus flow must be determined by the following equation:

$$\mathrm{Re}_{D_h} = \frac{4\dot{m}}{\pi\mu(D_{bore} + D_c)} \tag{2.7}$$

where D_c is the outer diameter of the drill string collar.

In analyzing the Reynolds numbers for the given range of flow rates, it was determined that the annular flow can be modeled as laminar with the values ranging from 458.78 to 917.56 as shown in Figure 2.3.

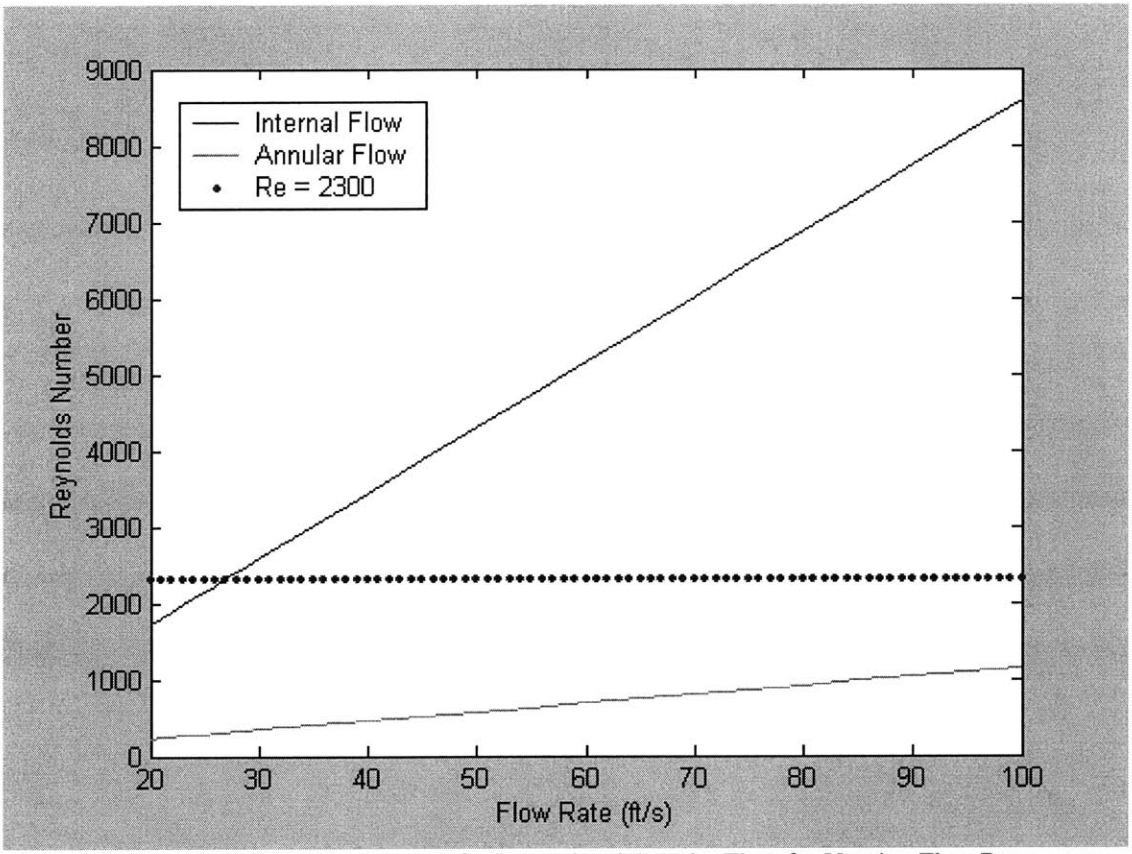

Figure 2.3. Reynolds Number for Internal and Annular Flow for Varying Flow Rates

When modeling laminar annular flows with constant heat flux from both surfaces, the Nusselt numbers for inner and outer surfaces are determined by:

$$Nu_i = \frac{Nu_{ii}}{1 - \left(\frac{q_o''}{q_i''}\right)\theta_i^*} \tag{2.8}$$

$$Nu_o = \frac{Nu_{oo}}{1 - \left(\frac{q_i''}{q_o''}\right)\theta_o^*} \tag{2.9}$$

where q_i'' and q_o'' are the heat fluxes for the inner and outer surfaces of the annulus, respectively. The values of Nu_{ii}, Nu_{oo}, θ_i^*, and θ_o^* vary within the different models with respect to the aspect ratio, r^*, of the annulus which is defined as

$$r^* = \frac{D_c}{D_{bore}}. \tag{2.10}$$

In this model, r^*, is determined to be 0.82. For this model with an adiabatic bore hole, q_o'' is set to 0 W/m^2. The following sections will discuss two possible models for the annular flow – fully developed flow and simultaneously developing flow.

2.1.2.1 Fully Developed Flow

Figure 2.4a shows the relationships for Nu_{ii} and Nu_{oo}, and Figure 2.4b shows the relationships for θ_i^*, and θ_o^* dependant on r^* for a fully developed laminar flow model given by Incropera and DeWitt [5].

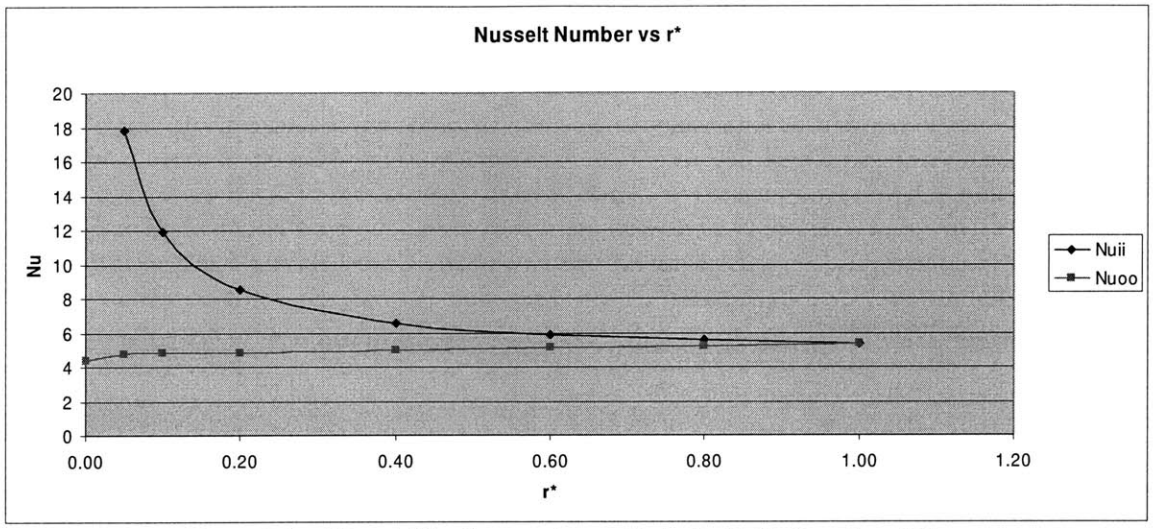

Figure 2.4a. Nusselt Number vs. Aspect Ratio for Fully Developed Flow

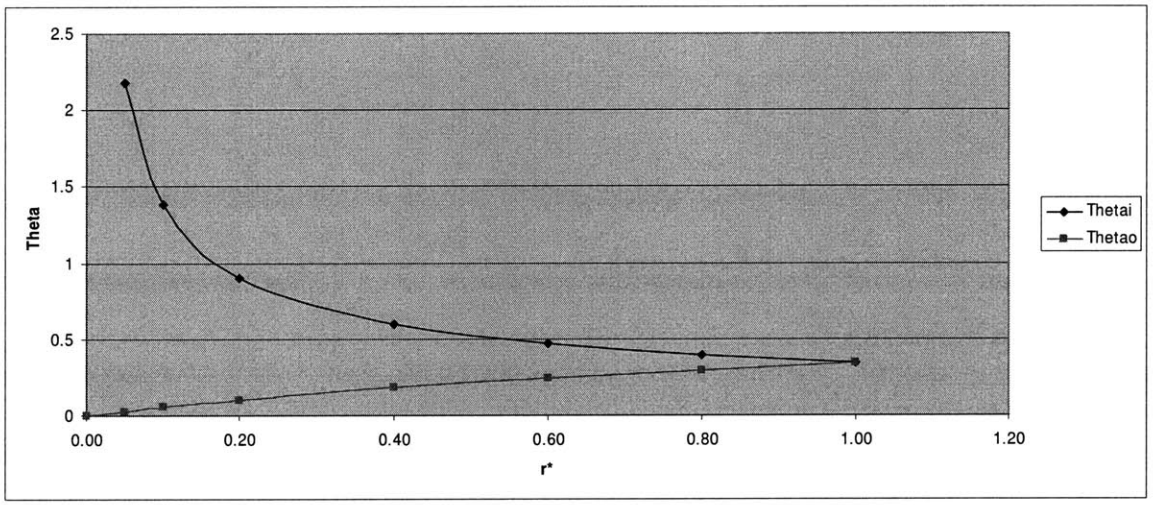

Figure 2.4b. Influence Coefficients vs. Aspect Ratio for Fully Developed Flow

In modeling the annular flow around the steering section where $r^* = 0.82$, the following values were obtained:

$$Nu_{ii} = 5.58$$
$$Nu_{oo} = 5.24$$
$$\theta_i^* = 0.401$$
$$\theta_o^* = 0.299$$

2.1.2.2 Simultaneously Developing Flow

This model represents an annular flow where the velocity and the temperature fields are developing simultaneously as given by Aung, Kakac, and Shah [6]. In this model the values of Nu_{ii}, Nu_{oo}, θ_i^*, and θ_o^* are dependent on r^* as well as the dimensionless axial distance, x^*, which is defined as:

$$x^* = \frac{L_k}{D_h Pe} \tag{2.11}$$

where L_k is the length from the entry point of the annulus through subassembly k of the steering section and Pe is the Peclet Number which is determined by:

$$Pe = \mathrm{Re}_{annulus} \mathrm{Pr}. \tag{2.12}$$

In this model, x^* varies with the location of the flow with respect to the steering section subassemblies.

Figure 2.5a and 2.5b show the relationships for Nu_{ii} and Nu_{oo} dependant on x^* for three values of r^*, .25, .5, and 1. Figure 2.6a and 2.6b show the relationships for θ_i^* and θ_o^* dependant of x^* for the same three values of r^*. Using these plots, the values for each subassembly was estimated for $r^* = 0.8$, as shown in Table 2.1.

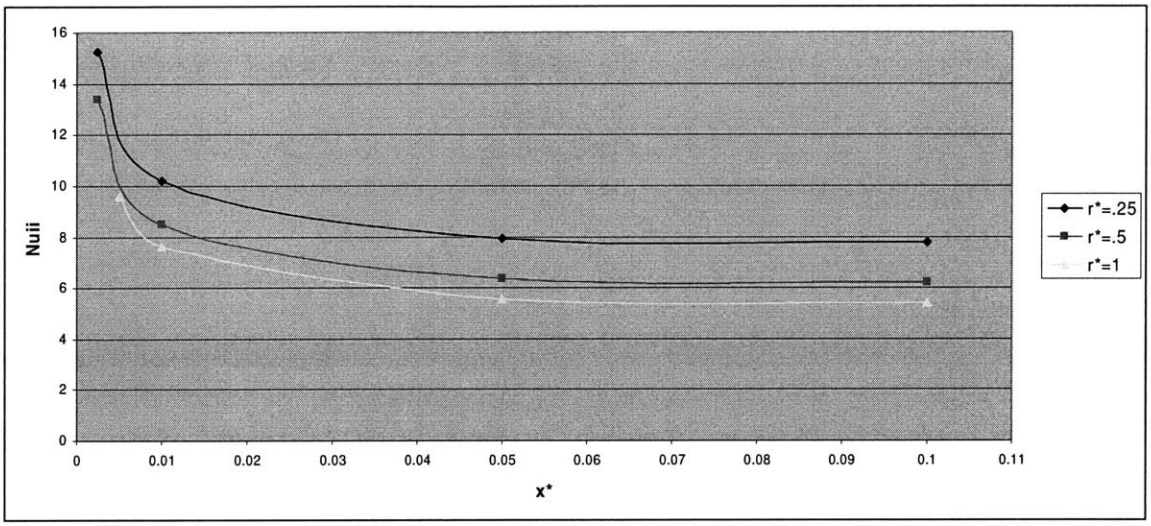

Figure 2.5a. Inner Surface Nusselt Number for Annular Flow vs. Dimensionless Axial Distance for Simultaneously Developing Flow

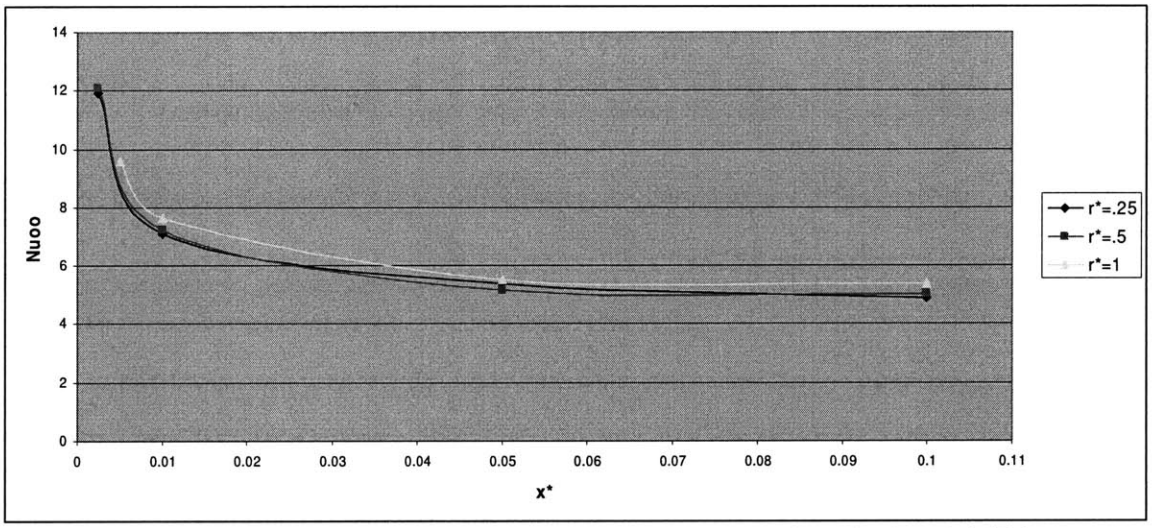

Figure 2.5b. Outer Surface Nusselt Number for Annular Flow vs. Dimensionless Axial Distance Simultaneously Developing Flow

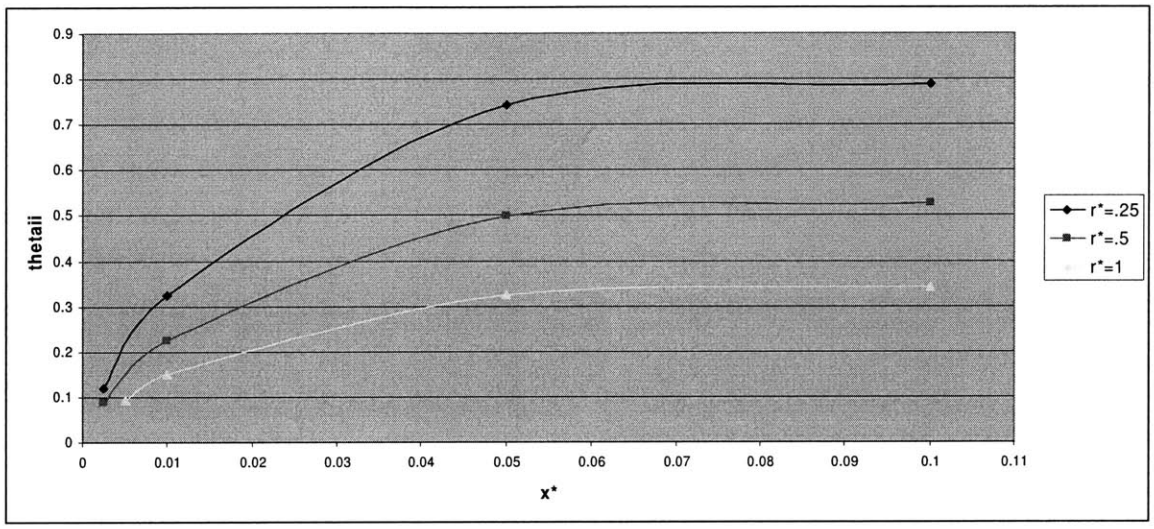

Figure 2.6a. Inner Surface Influence Coefficients for Annular Flow vs. Dimensionless Axial Distance Simultaneously Developing Flow

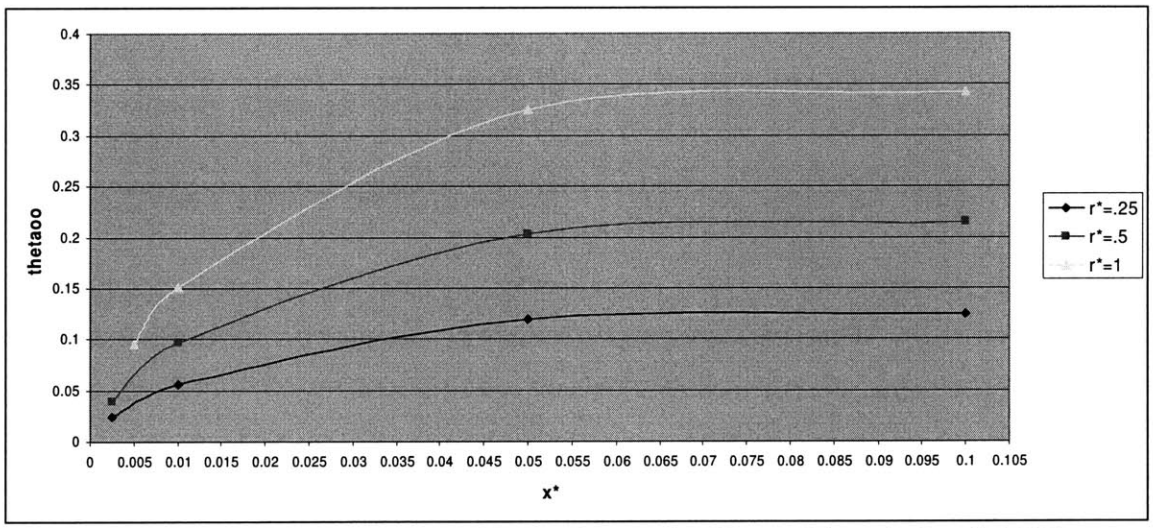

Figure 2.6b. Outer Surface Influence Coefficients for Annular Flow vs. Dimensionless Axial Distance Simultaneously Developing Flow

	L	Lcum	x*		Nuii	Nuoo	thetaii	thetaoo
Motor	0.285	1.587	0.088		5.3	5.2	0.44	0.30
GB	0.135	1.302	0.072		5.4	5.3	0.43	0.29
PC	0.413	1.167	0.064		5.5	5.4	0.41	0.28
OM	0.279	0.754	0.042		6.4	5.7	0.36	0.23
EOM	0.201	0.475	0.026		6.7	6.1	0.30	0.20
BS	0.170	0.273	0.015		7.3	6.8	0.24	0.16
TR	0.103	0.103	0.006		9.6	9.3	0.12	0.08
				AVG	**6.6**	**6.3**	**0.33**	**0.22**

Table 2.1. Average Nusselt Numbers and Influence Coefficients for Annular Flow

2.1.3 Heat Transfer Coefficients

The Nusselt numbers and the influence coefficients between the fully developed flow model and the simultaneously developing flow model are inconsistent. In this case, the latter model will be utilized. This point in the flow path is the initiation of the annular flow. Therefore, the velocity and temperature fields are simultaneously developing.

For the internal flow, Nu_D was determined to be 13.45. Using equation 2.6, h_i was determined to be 180.64 W/m^2K.

For the annular flow, Nu_{D_h} was estimated to be 6.6 from Table 2.1. Using equation 2.6 in terms of D_h, h_o was determined to be 118.14 W/m^2K.

2.2 Temperature Gradient of Mud Flow

In thermally analyzing the steering section, the focus for the design engineers is the temperature differentials within the mud flow and the effect of those bulk flow temperatures on the components within the tool. This will allow them to determine how the generated heat is dissipated into the mud flow, as well as determining the possible "hot spots" within the components of the tool. The motor section is of particular interest

because high temperatures may cause meltdowns in the electronic connections that link the motor to the control system within the electronic module.

The temperature gradient will be analyzed as a continuous flow as represented in Figure 2.7. In this diagram, the entry and exit temperatures are represented for each module of the steering section. $T_{i,ID}$, $T_{o,ID}$, $T_{i,OD}$, and $T_{o,OD}$ represents the internal entry temperature, internal exit temperature, annular entry temperature, and annular exit temperature, respectively. $T_{j,ID}$ and $T_{j,OD}$ for $j = [1,6]$ represent the entry and exit temperatures for the intermediate modules of the steering section. To clarify, for the internal flow, the exit temperature of one subassembly is equivalent to the entry

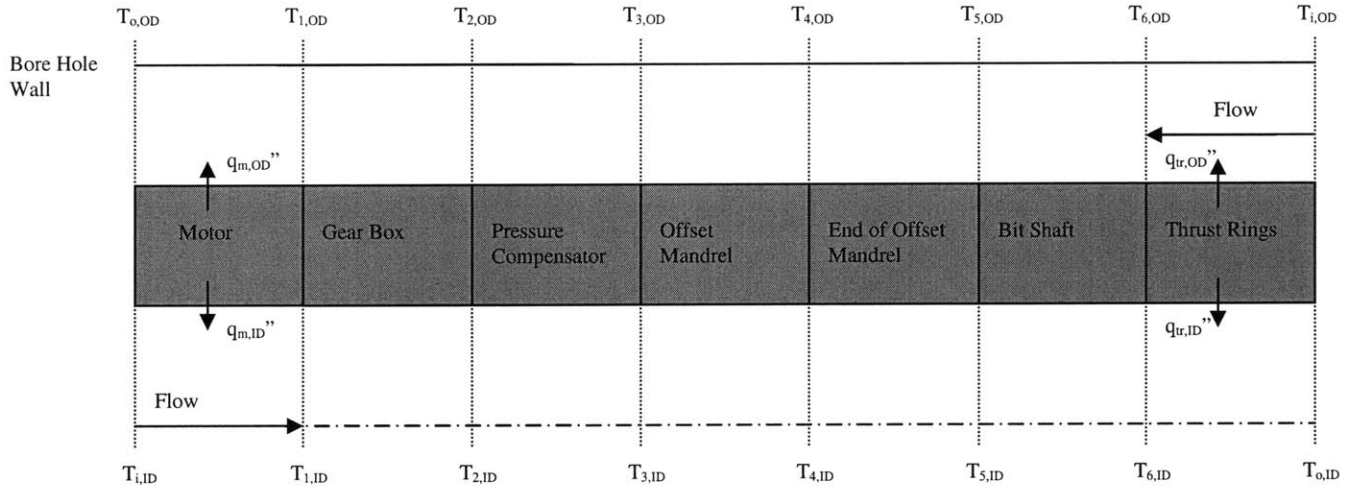

Figure 2.7. Model of Mud Flow Temperature Gradient

temperature of the following subassembly. For the annular flow, the entry temperature of one subassembly is equivalent to the exit temperature of the following subassembly. For example, $T_{2,ID}$ is the exit temperature of the gear box module and the entry temperature of the pressure compensator.

In order to begin the analysis, the boundary conditions of the flow must be stated. The entry temperature, $T_{i,ID}$, is given as a range from 150°C to 175°C, which will be dependent on the initial temperature of the mud when it enters the drill string as well as the amount of heat the mud has absorbed from other sections preceding the steering section, such as the electronics module, which is known to generate a significant amount of heat. For the purposes of this model and the focus of the analysis, $T_{i,ID}$ is defined within the range stated.

The second boundary condition is the exit temperature, $T_{o,OD}$. This temperature can be determined by:

$$T_{o,OD} = T_{i,ID} + \frac{Q_{tot}}{\dot{m} c_p} \tag{2.13}$$

where Q_{tot} is the total energy dissipated by the system, $\dot{m}$ is the mass flow rate, and c_p is the specific heat of the drilling mud. This determination of $T_{o,OD}$ assumes that the mud flow dissipates all the heat that is generated by the steering section and if applicable, the environment.

The third condition is the following equality:

$$T_{o,ID} = T_{i,OD}. \tag{2.14}$$

Since exiting internal flow becomes the entering annulus flow, the corresponding temperatures should be equal. Therefore, during the analysis, the results should agree with this condition. This takes into account the assumption that the energy dissipated from the drill bit is ignored.

2.1.3 Motor Section

Using an analysis already conducted by a member of the Advanced Drilling Group shown in Appendix A, the maximum energy dissipated by the motor, $Q_{m,tot}$, was determined to be 850 W. Because of the concentric annular orientation of oil drilling tools, the heat is dissipated to both the inner radius of the tool as well as the outer radius.

2.2.1.1 Stator

The main heat flux generation from the motor section comes from the stator of the motor. Because the stator was manufactured using a material with a high thermal conductivity, an assumption was made that the heat was distributed uniformly.

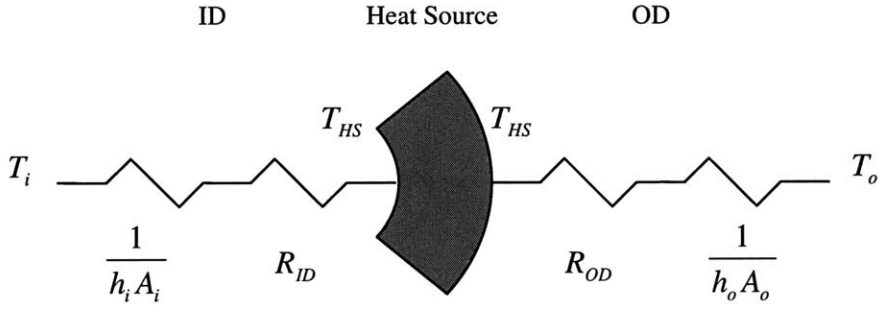

Figure 2.8. Temperature Distribution From Uniformly Distributed Heat Source

Therefore, in order to determine the independent heat dissipation to both the internal and annular flows, an assumption was made that the surface temperatures of the inner and outer surfaces of the stator were equivalent.

Figure 2.8 shows the temperature distribution from the surface of the heat source (the stator) to the internal and annular flows. T_{HS} denotes the temperature of the surface of the heat source. T_o and T_i denote the temperatures of the annular and internal flows respectively. R_{OD} and R_{ID} denote the total resistivity of the components of the motor section surrounding the stator. A_o and A_i denote the outer and inner surface areas the motor section.

The total energy of the motor, $Q_{m,tot}$, is found by summing the individual energies dissipated to both the annular flow and the internal flow:

$$Q_{m,tot} = Q_{m,OD} + Q_{m,ID} \tag{2.15}$$

The respective energies dissipated to the annular flow and internal flows are represented by:

$$Q_{m,OD} = \frac{T_{HS} - T_o}{R_{OD,tot}} \tag{2.16}$$

$$Q_{m,ID} = \frac{T_{HS} - T_i}{R_{ID,tot}} \tag{2.17}$$

where the total resistivities of the annular and the internal flow is determined by:

$$R_{OD,tot} = R_{OD} + \frac{1}{h_o A_o} \tag{2.18}$$

$$R_{ID,tot} = R_{ID} + \frac{1}{h_i A_i} \tag{2.19}$$

By substituting equations 2.16, 2.17, 2.18, and 2.19 into equation 2.15, T_{HS} can be determined by:

$$T_{HS} = \frac{R_{OD,tot} R_{ID,tot}}{R_{OD,tot} + R_{ID,tot}} \left[Q_{m,tot} + \frac{T_i}{R_{ID,tot}} + \frac{T_o}{R_{OD,tot}} \right]. \qquad 2.20$$

Because T_o and T_i are unknown, an initial value for T_{HS} can be estimated using the initial input temperature, $T_{i,ID}$, of 175°C (448°K) for T_i and the value for T_o which is determined by combining equations 2.13 and 2.15. Once the initial estimate for T_{HS} is determined, this value along with the initial values for T_o and T_i can be substituted into equations 2.16 and 2.17 to find the values for $Q_{m,OD}$ and $Q_{m,ID}$.

In order to obtain a more accurate estimate for T_{HS}, $Q_{m,OD}$, and $Q_{m,ID}$, the bulk flow temperature of the motor section for both the internal and the annular flow can be determined:

$$T_{b,ID} = \frac{T_{i,ID} + T_{1,ID}}{2} \qquad 2.21$$

$$T_{b,OD} = \frac{T_{o,OD} + T_{1,OD}}{2} \qquad 2.22$$

where $T_{1,ID}$ is the exit temperature from the motor section of the internal flow and $T_{1,OD}$ is the entry temperature of the motor section of the annular flow. These values can be determined by:

$$T_{1,ID} = T_{i,ID} + \frac{Q_{m,ID}}{\dot{m} c_p} \qquad 2.23$$

$$T_{1,OD} = T_{o,OD} - \frac{Q_{m,OD}}{\dot{m} c_p} \qquad 2.24$$

By using the bulk temperatures determined with equation 2.8 and 2.9 in place of T_o and T_i in equation 2.20, a new value for T_{HS} can be found. In order to obtain the best estimate possible, this process is repeated in order to iterate a converging value for T_{HS}.

Through the iteration process, the following values for the motor section were determined:

TbmID	176.74 degC
TbmOD	195.19 degC
Tstator	257.74 degC
QmID	336.93 W
QmOD	513.07 W

2.2.1.2 Rotor Shaft

Another concern in terms of heat dissipation from the motor is from the lubricating oil between the rotor shaft and the flex tube and between the rotor shaft and the stator. This Exxon ETO 25 high load carrying synthetic oil is under a maximum rotational velocity, ω_m, of the rotor shaft which is determined by:

$$\omega_m = 2\pi\omega_{bit}N \tag{2.25}$$

where ω_{bit} is the maximum rotational velocity of the bit shaft which is defined as 400 RPM and N is the gear ratio of the motor which is 8/3 by design.

In order to determine the heat dissipated from this oil as represented in Figure 2.9, the shear stress generated from the rotation was determined by:

$$\tau_{oil} = \mu_{oil}\frac{\omega_m D_{1,oil}}{2a} \tag{2.26}$$

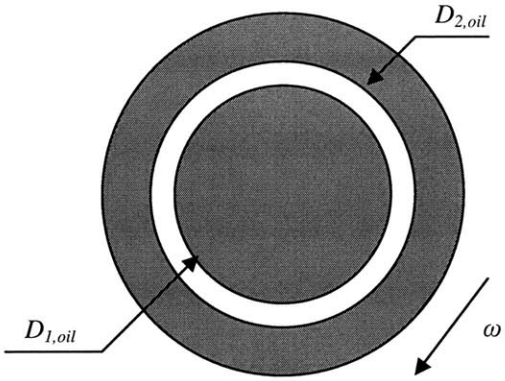

Figure 2.9. Oil Layer Around Rotor Shaft

where μ_{oil} is the viscosity of the oil which was determined to be $1.35*10^{-3}\ {}^{kg}/_{ms}$, $D_{1,oil}$ is the inner diameter, and a is the layer of oil between the rotor shaft and the flex tube represented by:

$$a = D_{2,oil} - D_{1,oil} \tag{2.27}$$

where $D_{2,oil}$ is outer diameter.

Using this shear stress, the generated torque was determined by:

$$T_{oil} = \frac{\pi\tau_{oil} D_{1,oil}^2 L_{rsh}}{2} \tag{2.28}$$

where L_{rsh} is the length of the rotor shaft. The power dissipated by the oil is represented by:

$$P = T_{oil}\omega_m \tag{2.29}$$

Using this equation, the power dissipated was determined to be a minimal 0.739 W between the rotor shaft and the flex tube and 34.93 W between the rotor shaft and the stator. Therefore, in the thermal analysis, the power dissipated by the oil is approximated

to be 36 *W* to the internal flow. The total heat dissipated to the internal flow is now 372.93 *W*.

2.2.2 Balanced Flow Heat Exchanger

In order to determine the following flow temperatures for both the internal and annular flows, the intermediate section must be analyzed. This section is modeled as a balanced flow heat exchanger. Because the annular flow temperature is modeled as the "hot" flow, heat is dissipated through the intermediate section of the tool and absorbed by the internal flow, which is modeled as the "cold" flow. The following relationship defines the heat that is dissipated in each subassembly *k*:

$$Q_{HE,k} = UA_k \frac{(T_{h,o} - T_{c,i}) - (T_{h,i} - T_{c,o})}{\ln\left(\frac{T_{h,o} - T_{c,i}}{T_{h,i} - T_{c,o}}\right)} \tag{2.30}$$

where $T_{h,i}$ and $T_{h,o}$ are the entry and exit temperatures of the annulus flow and $T_{c,i}$ and $T_{c,o}$ are the entry and exit temperatures of the internal flow for the corresponding subassembly *k*. UA_k is the overall heat transfer coefficient for each section *k* defined as:

$$UA_k = \frac{1}{\frac{1}{h_i A_{si,k}} + \frac{1}{h_o A_{so,k}} + R_k} \tag{2.31}$$

where h_i and h_o are the heat transfer coefficients of the internal and annular flows, respectively, $A_{si,k}$ and $A_{so,k}$ are the internal and annular heat transfer surface areas of subassembly *k*, respectively, and R_k is the overall resistivity of subassembly *k*. The derivations for resisitivity and values for R_k can be found in Appendix B.

Furthermore, $Q_{HE,k}$ can also be defined by the following two equations:

$$Q_{HE,k} = \dot{m}c_p\left(T_{h,o} - T_{h,i}\right) \tag{2.32}$$

$$Q_{HE,k} = \dot{m}c_p\left(T_{c,o} - T_{c,i}\right). \tag{2.33}$$

When solving for each subassembly in the intermediate section, $T_{c,i}$ and $T_{h,o}$ are known for they are solved for in the previous subassembly analysis. Therefore, solving equation 2.32 and 2.33 for $T_{c,o}$ and $T_{h,i}$ and substituting into equation 2.30 gives:

$$Q_{HE,k} = \frac{\dot{m}c_p\left(T_{h,o} - T_{c,i}\right)}{2}\left[1 - \exp\left\{-\frac{2UA_k}{\dot{m}c_p}\right\}\right]. \tag{2.34}$$

The cross sectional temperature differential defined as $T_{h,o} - T_{c,i}$ is constant throughout the entire intermediate section owing to the balanced flow and equation 2.32 and 2.33. Therefore, by defining this temperature differential as ΔT_{cs}, $Q_{HE,k}$ can be solved varying only by UA_k for each section *k*.

Once $Q_{HE,k}$ is determined, $T_{c,o}$ and $T_{h,i}$ can be solved utilizing equation 2.32 and 2.33.

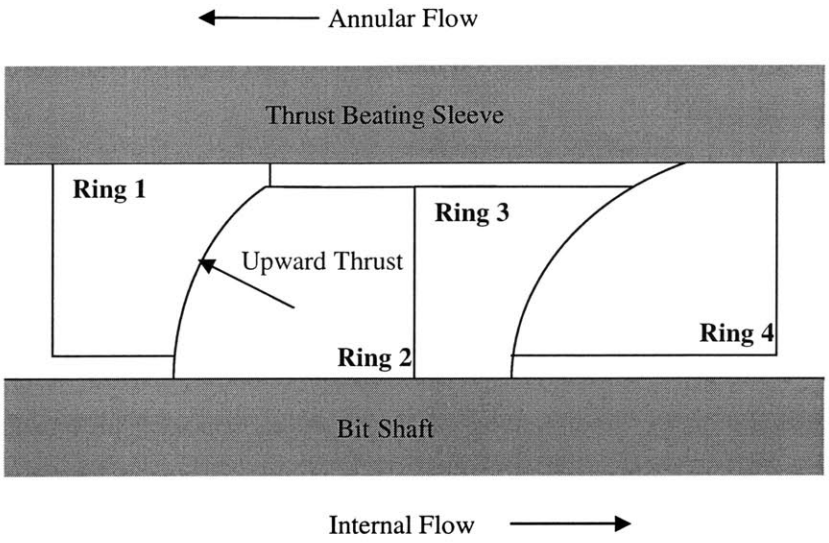

Figure 2.10. Sketch of Thrust Ring Configuration.

2.2.3 Thrust Ring Section

The thrust rings are configured as shown in Figure 2.10. The configuration of the four rings serves two purposes. The first two rings are designed to absorb the upward force due to the weight-on-bit during the drilling process. The latter two rings are designed to absorb any pulling force that may be generated during pullback processes of the tool. Pullback forces may occur while exiting the bore hole after drilling, during the drilling process when pullback is necessary to relieve the drilling area of debris, or during back reaming processes. For this thermal analysis, the heat generated from the first two rings will be the focus because force due to weight-on-bit while drilling is the dominant occurrence of the drilling process.

The frictional force generated by the contact between the thrust rings is determined by:

$$F_f = \mu_{tr} F_{WOB} \tag{2.35}$$

where μ_{tr} is coefficient of friction between the two thrust rings and F_{WOB} is the force due to the weight-on-bit. The coefficient of friction was estimated to be 0.1 and the maximum weigh-on-bit is 55 klbf or approximately 245 kN.

From this maximum frictional force, the total power dissipated is determined by

$$Q_{tr,tot} = F_f 2\pi R_f \omega_{bit} \tag{2.36}$$

where R_f is the radius of the path that the rotation that any given point on the interface between the two thrust rings follows, which is represented in Figure 2.11 where the arrow denotes the direction of rotation.

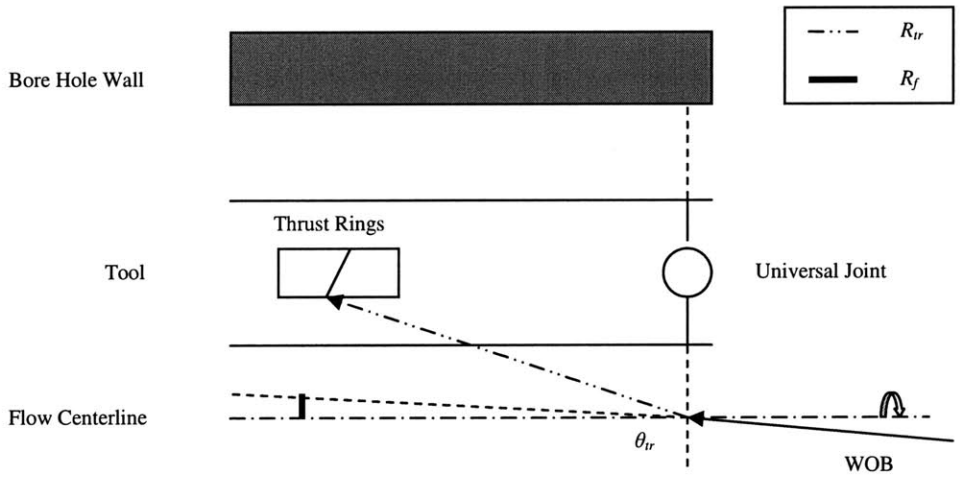

Figure 2.11. Diagram of Geometric Relationship of Thrust Rings and Load Bearing Bit Shaft

The universal joint allows an offset of θ_{tr} degrees off the centerline to allow for directional drilling. Using the geometric relationships, R_f can be determined by:

$$R_f = R_{tr} \sin(\theta_{tr}) \tag{2.37}$$

where R_{tr} is the radius of the arc of the two thrust rings. The maximum angular value, θ_{tr}, allowed by the universal joint is 0.6 degrees and the R_{tr} is 5 inches.

By utilizing equation 2.36, the power dissipated by the thrust rings due to the maximum weight-on-bit was determined to be 1364 *W*.

In order to determine the individual heat dissipation to the internal and annular flows, $Q_{tr,ID}$ and $Q_{tr,OD}$, the same process used in Section 2.2.1.1 is performed, using appropriate values for the thrust ring section. The initial T_{HS} is estimated by using the values for $T_{6,ID}$ and $T_{6,OD}$ for T_i and T_o for equation 2.20 which was determined from the balanced flow heat exchanger relationships. After finding the initial estimate for T_{HS}, $Q_{tr,ID}$, and $Q_{tr,OD}$, the same iterative process is followed and the following values for the thrust ring section were determined:

TbtrID	180.91 degC
TbtrOD	187.95 degC
Tthrust	433.97 degC
QtrID	439.02 W
QtrOD	924.98 W

2.3 Results

The analysis of the mud flow temperature gradients and the cross sectional temperature distributions were performed considering the system's worst-case-scenarios:

- Flow rate = 40 ft/s.
- Input flow temperature = 175 °C.
- Component heat flux at maximum levels.

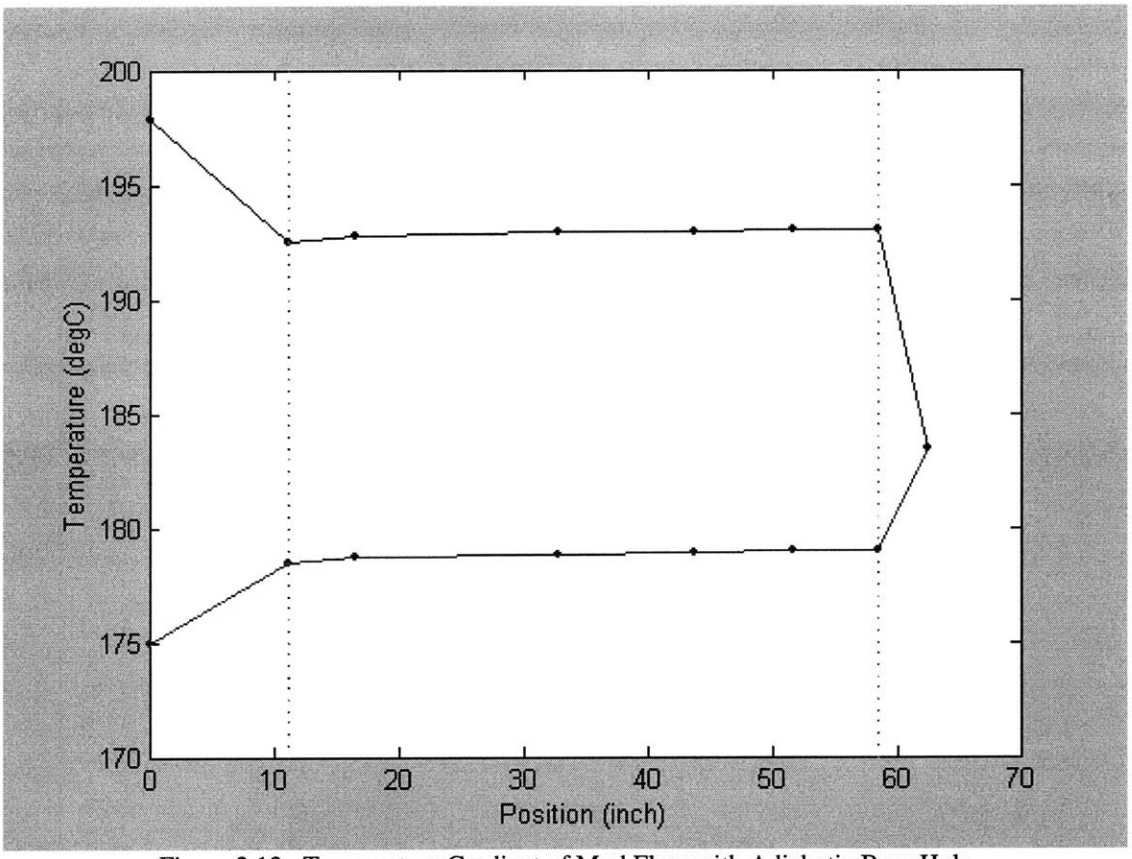

Figure 2.12. Temperature Gradient of Mud Flow with Adiabatic Bore Hole

2.3.1 Temperature Gradient Results

Figure 2.12 represents the temperature gradient of the drilling mud flow with an adiabatic bore hole. The internal entry point into the steering section is noted at (0 inch, 175°C) and the flow path follows the path of the graph to the right. The point at which a change in direction occurs represents the entry point into the annular flow path. The figure is subdivided into three sections which represent the motor section, the intermediate section, and the thrust ring section, in order from left to right.

In analyzing this plot, the largest temperature gradient occurs at the motor and thrust ring section, which is concurrent with the fact that these two sections generate the heat in the system. The exit temperature of this model is 198.19°C

An area of interest in this plot is the intermediate section. Figure 2.12 shows a typical pattern seen in a balanced flow heat exchanger. The temperature gradient of the internal mud flow, which in this case is the "cold" flow, increases while the gradient of the annular flow, or the "hot" flow, decreases. This is due to the energy from the "hot" annular flow being dissipated into the "cold" internal flow. Because the energy dissipated from the annular flow is equal but opposite from the energy absorbed by the internal flow, the cross sectional temperature differential is equal throughout the intermediate section. The energy dissipated by the annular flow and absorbed by the internal flow was found to be 47.71 *W*.

2.3.2 Cross Sectional Temperature Distribution

The cross sectional temperature distribution allows the engineer to analyze the temperature differentials between the different components of a chosen section. In order

to determine these cross sectional temperatures, the bulk flow temperatures determined in Section 2.2.1.1 and 2.2.3 will be used as the boundary conditions:

$$T_{b,m,ID} = \frac{T_{1,ID} + T_{i,ID}}{2} \tag{2.38}$$

$$T_{b,m,OD} = \frac{T_{o,OD} + T_{1,OD}}{2} \tag{2.39}$$

$$T_{b,tr,ID} = \frac{T_{o,ID} + T_{6,ID}}{2} \tag{2.40}$$

$$T_{b,tr,OD} = \frac{T_{6,OD} + T_{i,OD}}{2}. \tag{2.41}$$

By utilizing $Q_{m,ID}$, $Q_{m,OD}$, $Q_{tr,ID}$, $Q_{tr,OD}$, and the resistivities of the various layers within the two focus sections as described in Appendix B, the surface temperatures at each component interface are determined.

In analyzing the temperature differentials between the component layers of the motor section and the thrust ring section, several problem areas may be identified. In Figure 2.13a, the segments with very high temperature differentials represent the two oil layers used for lubricating the rotor shaft, an epoxy layer which attaches the motor housing to the stator, and an air gap between the drill collar and the motor housing. In Figure 2.13b, the air gap between the drill collar and the bearing sleeve represents the highest temperature differential in the thrust ring section. By identifying these areas, possible design changes may be put into place to decrease the resistivity between components and to improve the heat transfer mechanism. This will help to decrease the maximum temperatures within these components and may help to prevent any possible breakdowns.

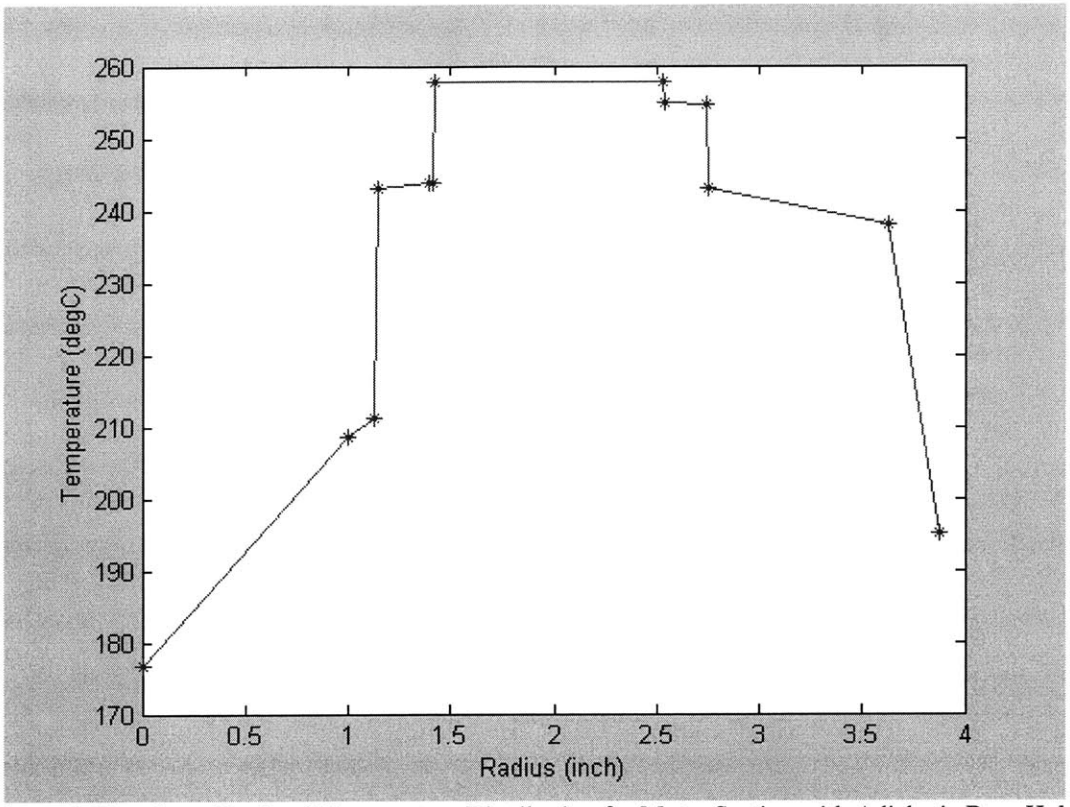

Figure 2.13a. Cross Sectional Temperature Distribution for Motor Section with Adiabatic Bore Hole

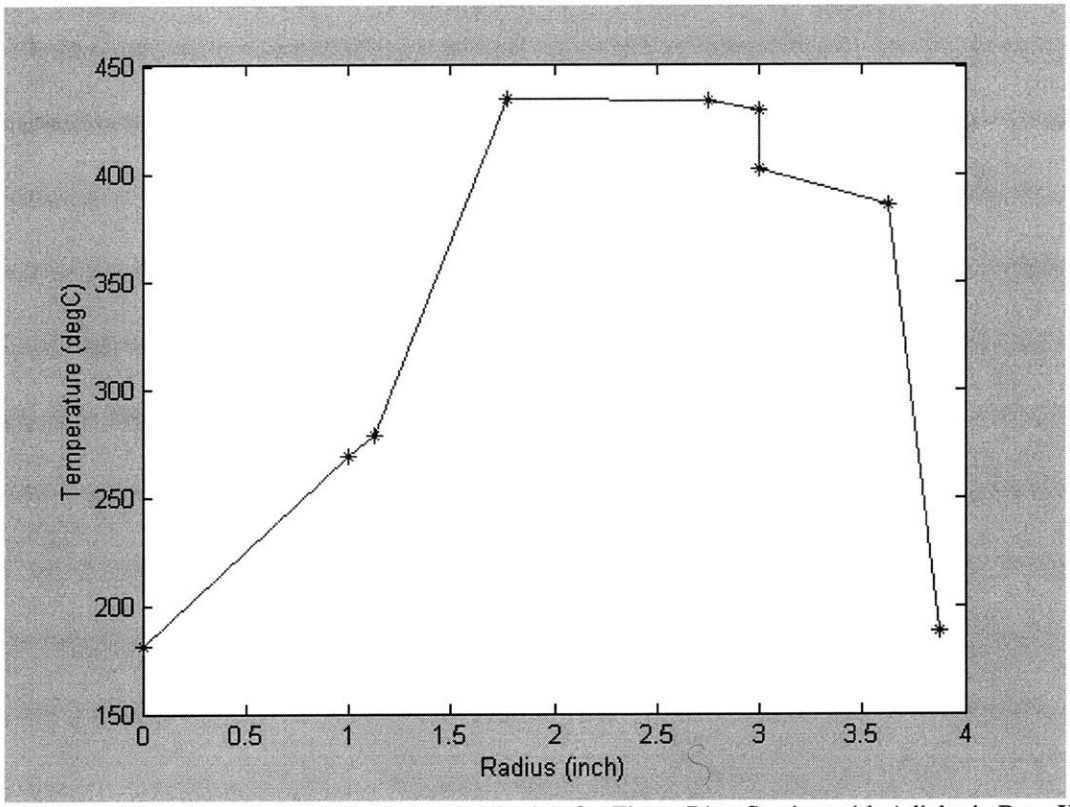

Figure 2.13b. Cross Sectional Temperature Distribution for Thrust Ring Section with Adiabatic Bore Hole

CHAPTER 3

THERMAL ANALYSIS – ENVIRONMENTAL HEAT FLUX

This analysis will now consider not only the heat generated within the tool, but also the environmental heat flux that may also affect the thermal state of the tool.

In order to determine the heat flux generated by the environment, we must first determine the shape factor of the bore hole configuration shown in Figure 3.1.

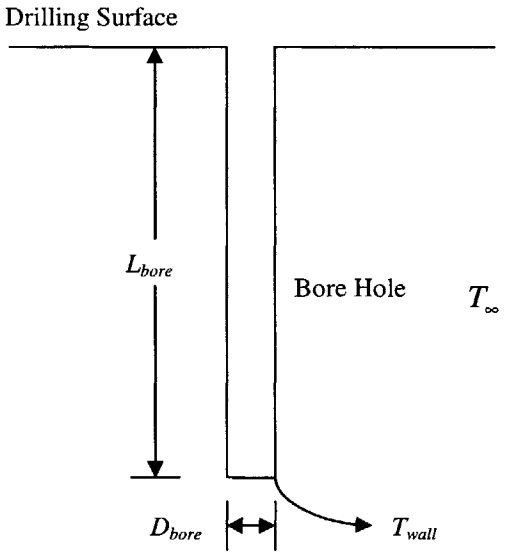

Figure 3.1. Diagram of Bore Hole

This shape factor is defined as:

$$S_f = \frac{2\pi L_{bore}}{\ln\left(\frac{4L_{bore}}{D_{bore}}\right)} \tag{3.1}$$

where L_{bore} and D_{bore} is the depth and the diameter of the borehole, respectively.

Using this shape factor the heat dissipated by the environment is

$$Q_{e,tot} = S_f k_e (\overline{T}_{wall} - T_\infty) \tag{3.2}$$

where k_e is the thermal conductivity of the material of the drilling environment, $\overline{T}_{wall}$ is the average temperature of the wall of the bore hole at the drilling depth which is unknown until internal conditions are taken into account. T_∞ is estimated to have a maximum value of 200°C at any given depth where $L_{bore} >> D_{bore}$.

To find the total heat flux, $Q_{e,tot}$ is divided by the total surface area of the borehole which gives:

$$q_e" = \frac{2k_e}{D_{bore}\ln\left(\frac{4L_{bore}}{D_{bore}}\right)}(T_{wall} - T_\infty). \tag{3.3}$$

This analysis takes into account only the environmental heat surrounding the steering section. Therefore this energy, Q_e, is defined as:

$$Q_e = q_e" A_{s,bore} \tag{3.4}$$

where $A_{s,bore}$ is the surface area of the bore hole wall surrounding only the steering section.

Because $\overline{T}_{wall}$ is not known, an approximation is made by taking the average temperature of the annular mud flow.

3.1 Temperature Gradient of Mud Flow with Environmental Influences

In this model, the total energy, Q_{tot}, now includes the total energy due to the environment in addition to the heat dissipated by the motor and the thrust rings:

$$Q_{tot} = Q_{m,tot} + Q_{tr,tot} + Q_e . \tag{3.5}$$

The energy dissipated from the surrounding environment around each subassembly k of the steering section, $Q_{e,k}$, is determined by:

$$Q_{e,k} = q_e'' A_{bore,k} \tag{3.7}$$

where $A_{bore,k}$ is the bore surface area surrounding a subassembly k of the steering section.

3.1.1 Motor Section

$T_{o,OD}$ can be found by substituting equation 3.5 into equation 2.13:

$$T_{o,OD} = T_{i,ID} + \frac{Q_{m,tot} + Q_{tr,tot} + Q_e}{\dot{m} c_p} \tag{3.6}$$

$T_{i,ID}$ is determined by using equation 2.23 because the same values for $Q_{m,ID}$ and $Q_{m,OD}$ as determined in Section 2.2.1.1. In order to determine $T_{1,OD}$, a variation must be made to equation 2.24:

$$T_{1,OD} = T_{o,OD} - \frac{Q_{m,OD} + Q_{m,e}}{\dot{m}c_p} \tag{3.8}$$

Since the annular flow is now exposed to both the tool heat flux and the environmental heat flux, this must be accounted for in the model.

3.1.2 Balanced Flow Heat Exchanger

The intermediate section is now analyzed. This section is again analyzed as a balanced flow heat exchanger. The heat dissipated to the internal flow is defined by 2.30. The overall heat transfer coefficient for each subassembly *k* is defined by equation 2.31

However, the environmental heat flux must also be taken into account. This energy, $Q_{e,k}$, is defined as:

$$Q_{e,k} = \dot{m}c_p(T_{h,o} - T_{h,i}) + \dot{m}c_p(T_{c,o} - T_{c,i}). \tag{3.9}$$

In order to solve for $Q_{HE,k}$, h_{ii} of the corresponding section *k* must also be determined by:

$$h_{ii,k} = \frac{k_{water} Nu_{ii}}{D_h\left[1 - \left(\frac{q_e'' A_{s,o}}{Q_{OD,k}}\right)\theta_i^*\right]}. \tag{3.10}$$

where $Q_{OD,k}$ is the heat being dissipated through the tool to the internal flow from the annular flow and $h_{ii,k}$ is the heat transfer coefficient of the inner surface of the annular flow.

$Q_{OD,k}$ has the following balanced flow heat exchanger relationship with $Q_{HE,k}$:

$$Q_{HE,k} = -Q_{OD,k} \tag{3.11}$$

By solving equation 3.9 for the unknown cross sectional temperature differential, $T_{h,i} - T_{c,o}$, and substituting into the modified equation 2.30 along with equation 2.31 and 3.10, the following equation for $Q_{HE,k}$ is determined:

$$Q_{HE,k} = \frac{-h_i A_{si,k} A_{so,k} \left(q_e'' D_h \theta_i^* - k_{water} Nu_{ii} \Delta T\right)}{D_h h_i A_{si,k} + k_{mud} Nu_{ii} A_{so,k} + R_k k_{mud} Nu_{ii} A_{so,k} h_i A_{si,k}} \tag{3.12}$$

where $A_{si,k}$ and $A_{so,k}$ are the inner and outer surface areas of subassembly k. The Nusselt numbers and the influence coefficient have already been determined in Section 2.1.2.2 as average values through the entire length of the steering section. ΔT is defined to be:

$$\Delta T = \frac{\dfrac{-Q_{e,k}}{\dot{m} c_p}}{\ln\left[\dfrac{T_{h,o} - T_{c,i} - \dfrac{Q_{e,k}}{\dot{m} c_p}}{T_{h,o} - T_{c,i}}\right]} \tag{3.13}$$

Once $Q_{HE,k}$ is determined, $T_{h,i}$ and $T_{c,o}$ are determined by:

$$T_{h,i} = T_{h,o} - \frac{Q_{e,k} - Q_{HE,k}}{\dot{m} c_p} \tag{3.14}$$

$$T_{c,o} = T_{c,i} + \frac{Q_{HE,k}}{\dot{m} c_p}. \tag{3.15}$$

3.1.3 Thrust Ring Section

The final unknown temperatures $T_{o,ID}$ can be determined using $Q_{tr,ID}$ in place of $Q_{m,ID}$ in equation 2.23 and $T_{i,OD}$ can be solved by utilizing equation 2.24 with a variation in the total energy:

$$T_{i,OD} = T_{6,OD} - \frac{Q_{tr,OD} + Q_{tr,e}}{\dot{m}c_p}. \qquad 3.16$$

Values for $Q_{tr,ID}$ and $Q_{tr,OD}$ were determined in Section 2.2.3.

3.2 Results

The analysis of the mud flow temperature gradient and the cross sectional temperature distributions were performed considering the same conditions as stated in Section 2.3

3.2.1 Temperature Gradient Results with an Environmental Heat Flux

Figure 3.2 represents the temperature gradient of the drilling mud flow with the effects of an environmental heat flux. Once again, the largest temperature gradients occur at the motor and thrust ring sections. The exit temperature of this model is 202.41°C.

However, the intermediate section reveals a slightly different shape from what is expected from a balanced heat flow exchanger model. Since there exists an environmental heat flux, energy is being absorbed by both the annular flow and the internal flow. Therefore, the temperature gradients of both flows are increasing. The annular flow absorbs the heat dissipated by the bore hole walls. In turn, some of this

energy absorbed by the annular "hot" flow is now dissipated into the internal "cold" flow through the tool itself causing the internal flow temperature gradient to rise. This model indicates that the internal flow gains 64.35 W and the annular flow gains 244.65 W of energy from the environment.

Because in real-world drilling cases, an environmental heat flux exists, the gradient represented by Figure 3.2 is more accurate. However, because the depth of drilling is very deep, the $q_e"$ is relatively small compared to the total heat flux generated by the tool components. Therefore, the environmental heat flux does not have a great effect on the overall temperature gradient. The temperature difference between the flow exiting the steering section between the environmental heat flux model and the adiabatic bore hole model from Chapter 2 is 4.22°C. The main difference lies in the heat dissipation trends in the intermediate sections.

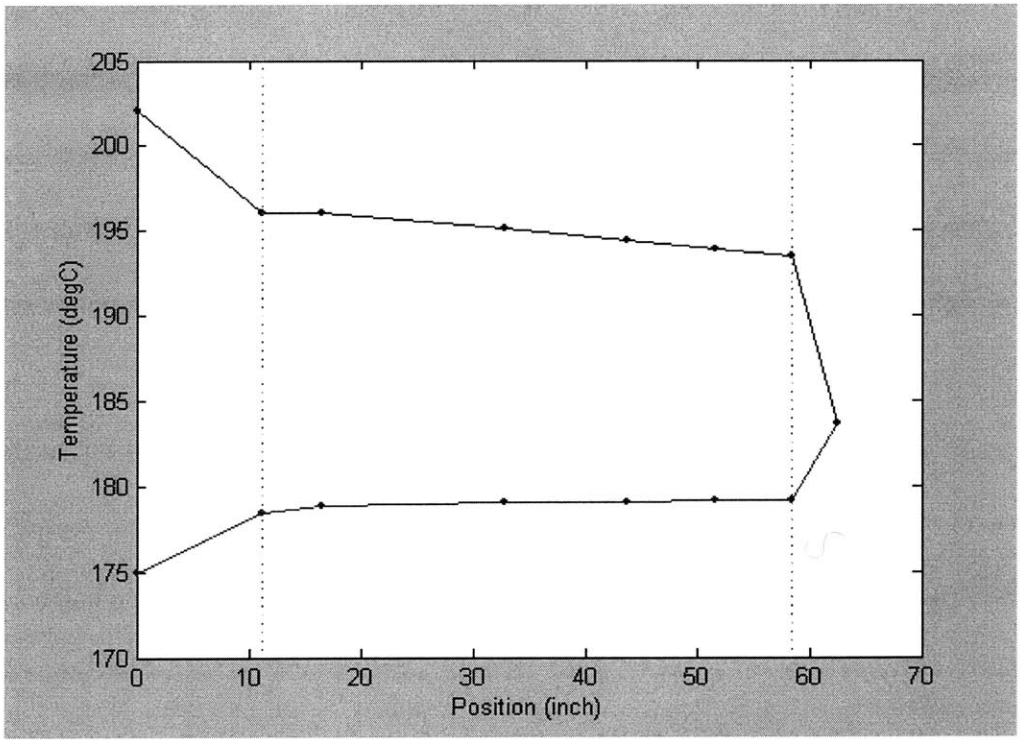

Figure 3.2. Temperature Gradient of Mud Flow with Environmental Heat Flux

3.2.2 Cross Sectional Temperature Distribution Results

The cross sectional temperature distribution for the environmental heat flux model follow the same trends as the adiabatic bore hole model. In the motor, the largest temperature differentials exist in the two oil layers that lubricate the rotor shaft, the epoxy layer that attaches the motor housing to the stator and the air gap between the drill collar and the motor housing. In the thrust ring section, the air gap between the drill collar and the bearing sleeve represents the highest temperature differential. Once again, this shows that possible design changes can increase the efficiency of heat dissipation in these two subassemblies.

One observation from these plots is that there exists a slight differential within the stator of the motor tending towards the annular flow. This may be due to the fact that the heat being absorbed by the annular flow from the environment is having an effect on the heat dissipation towards the annular flow. However, there only exists a slight gradient in the thrust rings. This implies that the heat is uniformly distributed and that the environmental heat flux is not having a significant effect. Because the length of the thrust rings is very small, the surface area that the environmental heat flux is exposed to is rather small. Therefore, the effect of the environmental heat flux on the heat dissipation in the thrust ring section is insignificant.

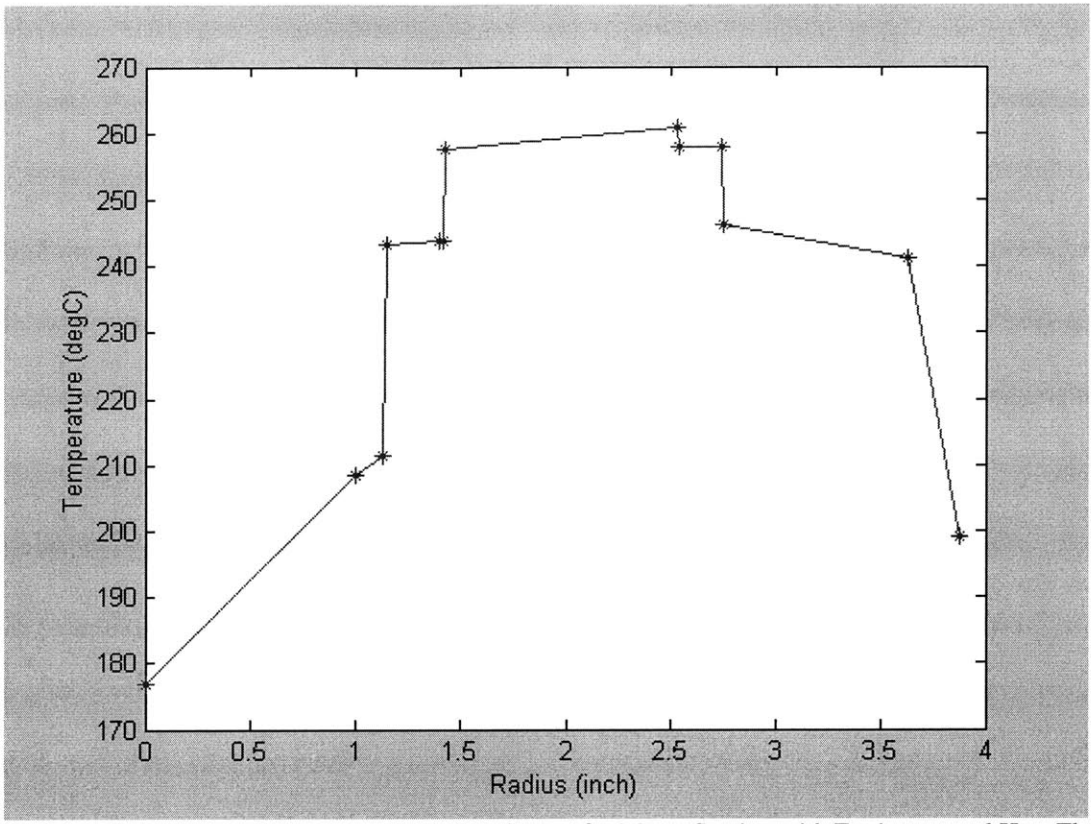

Figure 3.3a. Cross Sectional Temperature Distribution for Motor Section with Environmental Heat Flux

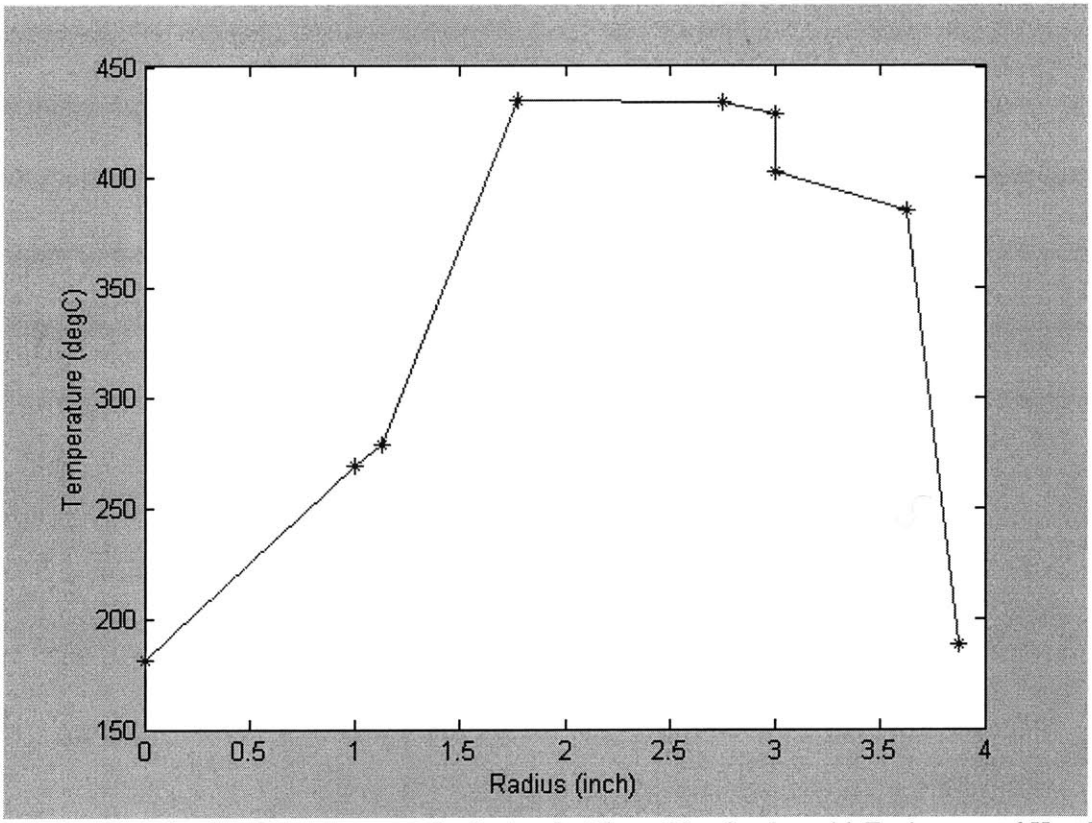

Figure 3.3b. Cross Sectional Temperature Distribution for Thrust Ring Section with Environmental Heat Flux

3.2.3 Comparison to the Adiabatic Bore Hole Model

In comparing the temperature gradient of the adiabatic bore hole model in Figure 2.12 and the temperature gradient of the environmental heat flux model in Figure 3.2 shows that there is only a slight difference in the final temperature. The main difference lies in the intermediate section where the tool acts as a balanced flow heat exchanger. This implies that the environmental heat flux plays a very insignificant role in the thermal state of the drilling mud during operation. Because of this slight difference, either models give good approximations for bulk flow temperatures around the focus sections of the analysis which are used for further analysis on the thermal state of the internal components.

In comparing the cross sectional temperature distribution, again, there is only a slight difference in the magnitudes of the temperatures where the environmental heat flux model temperatures are only slightly higher. Both models predict similar trends in the heat dissipation.

From this comparison, it can be concluded that the environmental heat flux has an insignificant effect on the thermal state of the tool.

3.3 Effect of Variance of Controllable Parameters

The only controllable parameters by the operator of the tool are the flow rate of the mud flow and the input temperature. However, these parameters can have very significant effects on thermal characteristics of the mud flow and the tool. Figure 3.4a and Figure 3.4b shows that the variance of flow rates significantly affects the internal surface temperature of the motor and thrust ring section. The effect is not as significant with the annular surface temperatures of the tool. However, as the flow rates increase,

the surface temperature for all components seems to level off at different values. Within the range specified in the tool design (40 ft/s to 80 ft/s), the figures demonstrate that a variance in flow rates have a minimal effect on the surface temperatures.

Figure 3.5a and Figure 3.5b shows the surface temperature dependant on the input mud flow temperature. These figures demonstrate that the surface temperatures will linearly increase with an increase in input temperature. For optimal heat dissipation, the mud flow should be pumped into the drill string at its lowest possible level.

In comparing the results for both the adiabatic bore hole model and the environmental heat flux model, the difference in results are once again insignificant. This is due to the same reason that there was small variance with the cross sectional temperature distributions between the two models.

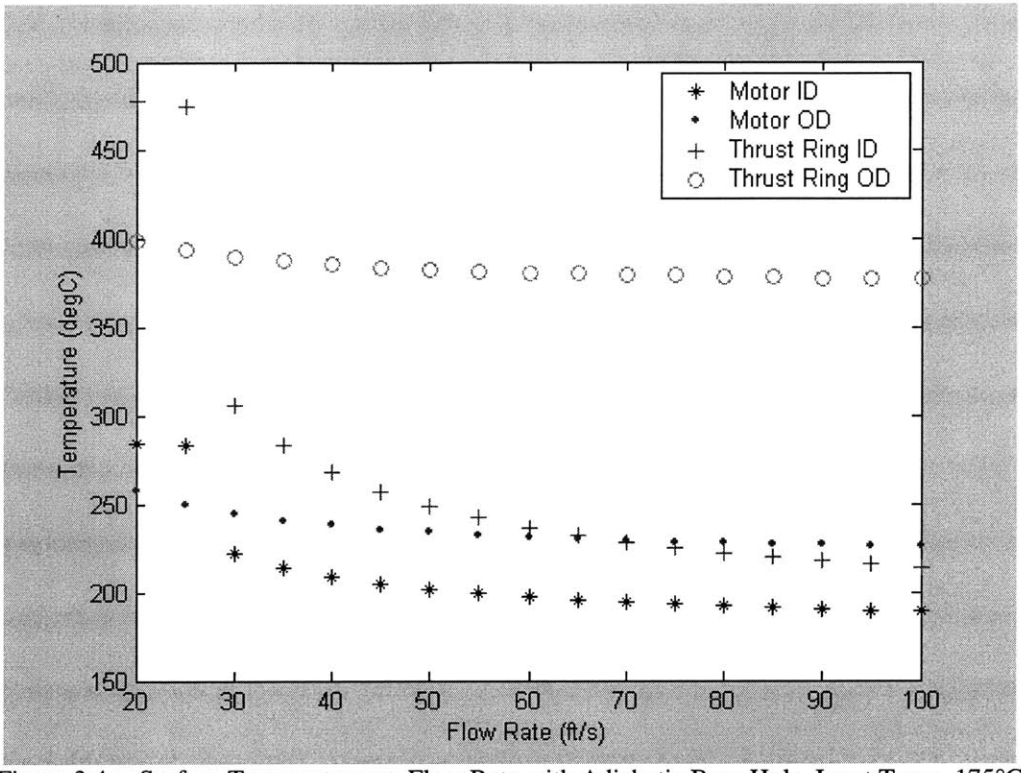

Figure 3.4a. Surface Temperature vs. Flow Rate with Adiabatic Bore Hole, Input Temp. 175°C

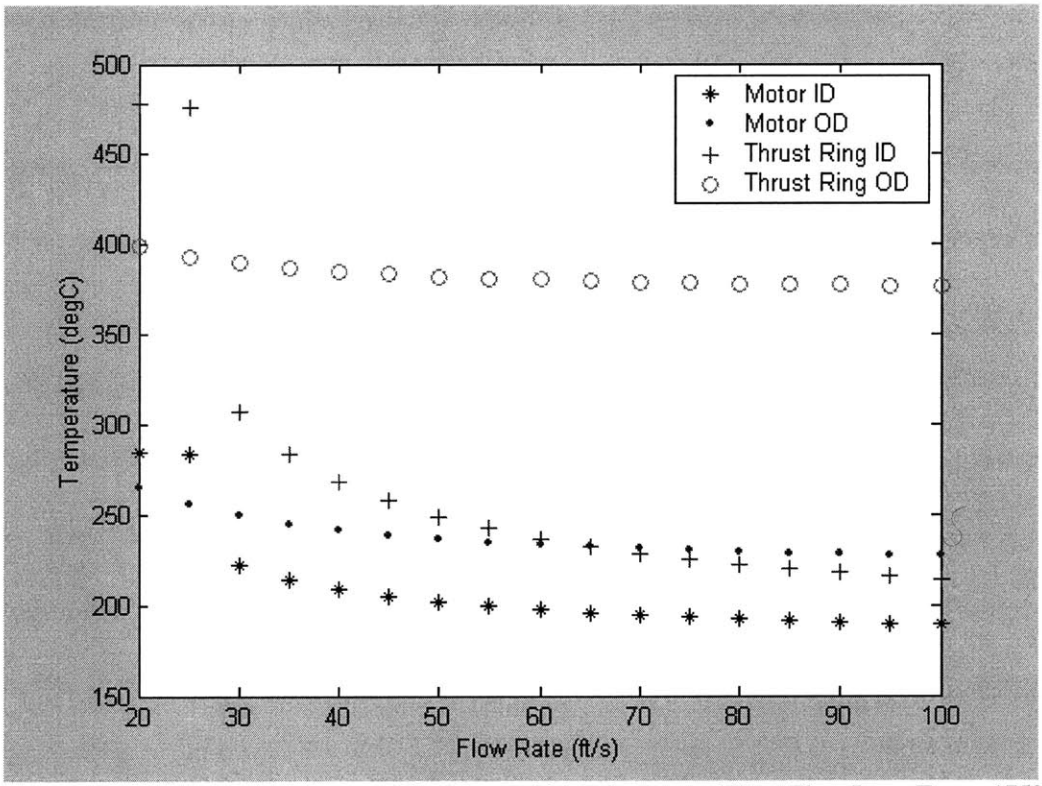

Figure 3.4b. Surface Temperature vs. Flow Rate with Environmental Heat Flux, Input Temp. 175°C

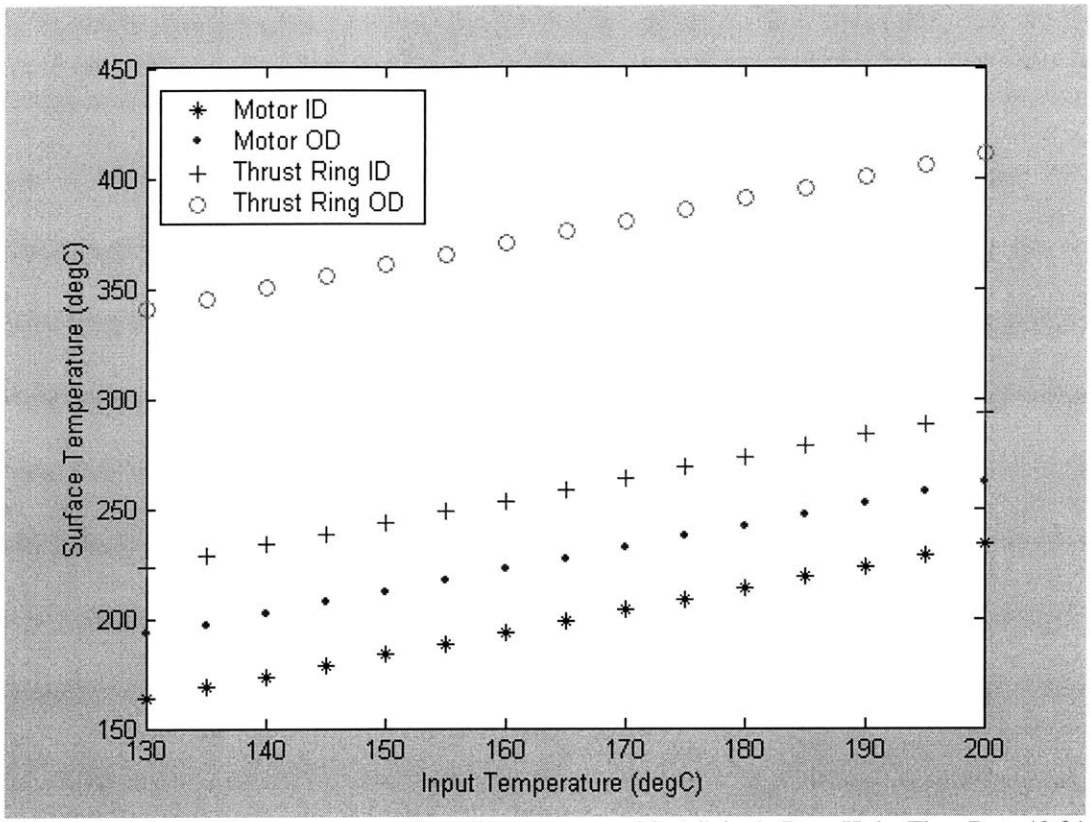

Figure 3.5a. Surface Temperature vs. Input Temperature with Adiabatic Bore Hole, Flow Rate 40 ft/s

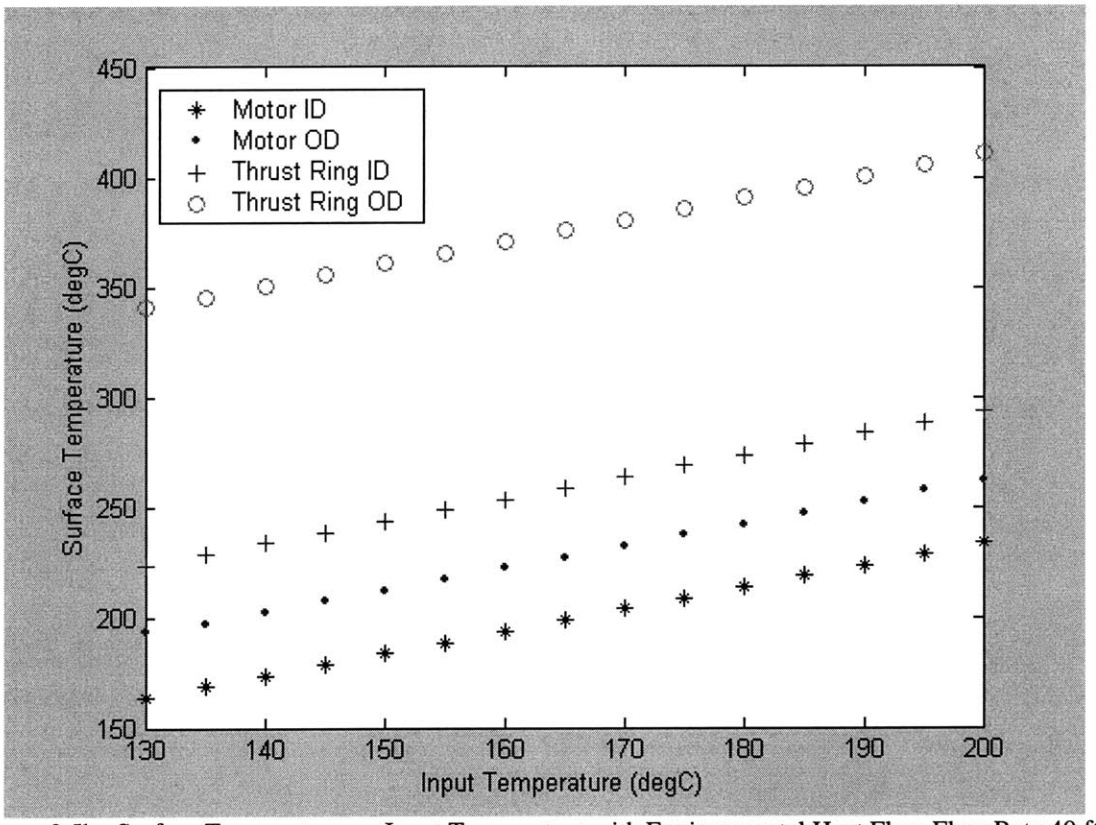

Figure 3.5b. Surface Temperature vs. Input Temperature with Environmental Heat Flux, Flow Rate 40 ft/s

CHAPTER 4

THERMAL ANALYSIS OF MOTOR SECTION

The motor section is of particular interest due to its electrical components that connect it to the electronics module. If the heat generated by the stator of the motor is not dissipated efficiently, the build up of heat may cause meltdowns with the wire insulations and consequently cause a system failure. In order to obtain a more detailed understanding of the heat distribution in the motor section, a finite difference analysis was conducted.

4.1 Finite Difference Analysis

The finite difference equations for the nodal temperatures were obtained by utilizing the conservation of energy principle to the control volumes surrounding the node as shown in Figure 4.1.

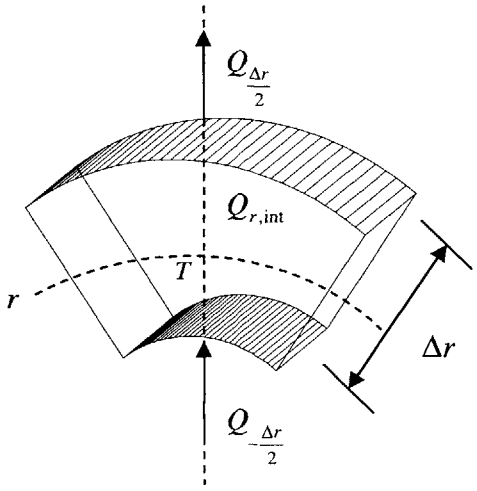

Figure 4.1. Control Volume for Finite Difference Analysis

In this model, the energy transfer in the axial direction (z-direction) and azimuthal direction (θ-direction) were considered to be non-applicable due to the assumption that there exists axial and azimuthal symmetry. Axial symmetry is assumed because the bulk flow temperatures are being used for the boundary conditions along the entire length of the motor section. Therefore, the energy balance equation considers only the energy transfer in the radial direction (r-direction):

$$Q_{\frac{\Delta r}{2}} + Q_{-\frac{\Delta r}{2}} + Q_{r,\text{int}} = 0 \qquad 4.1$$

where $Q_{\frac{\Delta r}{2}}$ is the energy transfer out of the control volume through the outer radius, $Q_{-\frac{\Delta r}{2}}$ is the energy transferred into the control volume through the inner radius, and $Q_{r,\text{int}}$ is the internal energy generated by the control volume.

The following subsections will discuss the derivations for the finite difference equations for conduction within one material, interface conduction between two materials, and internal and annular flow convection.

4.1.1 Conduction

The energy transferred through conduction within one material was determined by utilizing Fourier's law for conduction:

$$\dot{q} = -k\frac{\partial T}{\partial r} \tag{4.2}$$

where $\dot{q}$ is the heat flux and k is the thermal conductivity of the material.

Utilizing this equation, the energy transferred between the outer and inner radial surfaces were determined to be:

$$Q_{\frac{\Delta r}{2}} = k\left(\frac{T_r - T_{r+\frac{\Delta r}{2}}}{\Delta r}\right)2\pi\left(r+\frac{\Delta r}{2}\right)\Delta z \tag{4.3}$$

$$Q_{\frac{\Delta r}{2}} = k\left(\frac{T_{r-\frac{\Delta r}{2}} - T_r}{\Delta r}\right)2\pi\left(r-\frac{\Delta r}{2}\right)\Delta z\,. \tag{4.4}$$

In the stator, each control volume generates its own energy, $Q_{r,\text{int}}$, which is determined by:

$$Q_{r,\text{int}} = 2\pi r\Delta r\Delta z\dot{q}_v \tag{4.5}$$

where $\dot{q}_v$ is the energy per unit volume of the stator. For the stator, the $\dot{q}_v$ is estimated to be approximately 336 kW/m^3.

By substituting equations 4.3, 4.4, and 4.5 into the energy balance equation, the following relationship for the nodal temperature for conduction is derived:

$$T_r = \frac{1}{2r}\left[\left(r+\frac{\Delta r}{2}\right)T_{r+\frac{\Delta r}{2}} + \left(r-\frac{\Delta r}{2}\right)T_{r-\frac{\Delta r}{2}}\right] + \frac{\Delta r^2}{2k}\dot{q}_v\,. \tag{4.6}$$

If the relationship for conduction is used when no internal heat generation is present, the last term in equation 4.6 is set to zero.

4.1.2 Interface Conduction Between Two Materials

For the control volumes whose respective outer and inner radial surfaces form an interface between two materials as shown in Figure 4.2, the energy transfer through two different thermal conductivities must be determined.

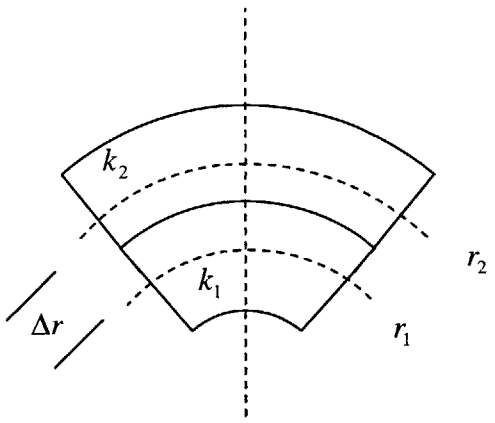

Figure 4.2. Interface Control Volumes Between Two Materials.

The total resistivity between the two nodes is represented by the sum of the resistivities through each material:

$$R_{tot} = R_{k_1} + R_{k_2} \tag{4.7}$$

where the resistivities of each layer is determined by:

$$R_{k_1} = \frac{\ln\left(\frac{r_1 + \frac{\Delta r}{2}}{r_1}\right)}{2\pi k_1 \Delta z} \tag{4.8}$$

$$R_{k_2} = \frac{\ln\left(\frac{r_2}{r_2 - \frac{\Delta r}{2}}\right)}{2\pi k_2 \Delta z} \tag{4.9}$$

By substituting in equations 4.8 and 4.9 into equation 4.7, the total resistivity between the two nodes is determined by:

$$R_{tot} = \frac{1}{2\pi \Delta z k_1 k_2} \ln\left(\frac{r_*^{k_2 - k_1} r_2^{k_1}}{r_1^{k_2}}\right) \tag{4.10}$$

where r_* is the radius of the interface surface represented by:

$$r_*^1 = \left(r_1 + \frac{\Delta r}{2}\right) \tag{4.11a}$$

$$r_*^2 = \left(r_2 - \frac{\Delta r}{2}\right) \tag{4.11b}$$

where equation 4.11a is used when determining the nodal temperature in control volume 1 and equation 4.11b is used when determining the nodal temperature in control volume 2.

When determining the nodal temperature in control volume 1, the energy transfer through the interface surface is determined by:

$$Q_{\frac{\Delta r}{2}} = \frac{T_r - T_{r+\frac{\Delta r}{2}}}{R_{tot}}. \tag{4.12}$$

By substituting equation 4.4 and 4.12 into the energy balance equation, the relationship for the nodal temperature in control volume 1 is:

$$T_r = \frac{1}{\dfrac{k_2}{\ln\left(\dfrac{r_*^{k_2-k_1} r_2^{k_1}}{r_1^{k_2}}\right)} + \dfrac{\left(r_1 - \dfrac{\Delta r}{2}\right)}{\Delta r}} \left[\frac{k_2}{\ln\left(\dfrac{r_*^{k_2-k_1} r_2^{k_1}}{r_1^{k_2}}\right)} T_{r+\frac{\Delta r}{2}} + \frac{\left(r_1 - \dfrac{\Delta r}{2}\right)}{\Delta r} T_{r-\frac{\Delta r}{2}} \right] \tag{4.13}$$

If an internal heat generation exists in control volume 1 as does in the outer radial control volumes of the stator, equation 4.5 is included into the energy balance equation and the nodal temperature is represented by:

$$T_r = \frac{1}{\dfrac{k_1 k_2}{\ln\left(\dfrac{r_*^{k_2-k_1} r_2^{k_1}}{r_1^{k_2}}\right)} + \dfrac{k_1\left(r_1 - \dfrac{\Delta r}{2}\right)}{\Delta r}} \left[\frac{k_1 k_2}{\ln\left(\dfrac{r_*^{k_2-k_1} r_2^{k_1}}{r_1^{k_2}}\right)} T_{r+\frac{\Delta r}{2}} + \frac{k_1\left(r_1 - \dfrac{\Delta r}{2}\right)}{\Delta r} T_{r-\frac{\Delta r}{2}} + r\Delta r \dot{q}_v \right] \tag{4.14}$$

For the nodal temperature of control volume 2, the energy transfer through the interface surface is determined by:

$$Q_{\frac{\Delta r}{2}} = \frac{T_{r+\frac{\Delta r}{2}} - T_r}{R_{tot}}. \tag{4.15}$$

By substituting equation 4.3 and 4.15 into the energy balance equation, the nodal temperature for control volume 2 is determined by:

$$T_r = \frac{1}{\dfrac{k_1}{\ln\left(\dfrac{r_*^{k_2-k_1} r_2^{k_1}}{r_1^{k_2}}\right)} + \dfrac{\left(r_2 + \dfrac{\Delta r}{2}\right)}{\Delta r}} \left[\frac{\left(r_2 + \dfrac{\Delta r}{2}\right)}{\Delta r} T_{r+\frac{\Delta r}{2}} + \frac{k_1}{\ln\left(\dfrac{r_*^{k_2-k_1} r_2^{k_1}}{r_1^{k_2}}\right)} T_{r-\frac{\Delta r}{2}} \right] \qquad 4.16$$

If an internal heat generation exists in control volume 2 as does in the inner radial control volume of the stator, equation 4.5 is once again included into the energy balance equation which gives:

$$T_r = \frac{1}{\dfrac{k_1 k_2}{\ln\left(\dfrac{r_*^{k_2-k_1} r_2^{k_1}}{r_1^{k_2}}\right)} + \dfrac{k_2\left(r_2 + \dfrac{\Delta r}{2}\right)}{\Delta r}} \left[\frac{k_2\left(r_2 + \dfrac{\Delta r}{2}\right)}{\Delta r} T_{r+\frac{\Delta r}{2}} + \frac{k_1 k_2}{\ln\left(\dfrac{r_*^{k_2-k_1} r_2^{k_1}}{r_1^{k_2}}\right)} T_{r-\frac{\Delta r}{2}} + r\Delta r \dot{q}_v \right] . \qquad 4.17$$

4.1.3 Convection

For the control volumes that border with the internal and annular flows, the nodes are located such that the nodal temperature relationships give the surface temperatures resulting from the interaction with the bulk flow temperatures. In the following derivations, the internal heat generation will be ignored because the heat generation in the modeling of the motor section is isolated to conduction in the stator and its respective interfaces.

The heat transfer through the surface interacting with the internal flow and the annular flow is determined by:

$$Q_{h_i} = h_i(T_{b,i} - T_r)2\pi r\Delta z \tag{4.18}$$

$$Q_{h_o} = h_o(T_r - T_{b,o})2\pi r\Delta z \tag{4.19}$$

where $T_{b,i}$ and $T_{b,o}$ is the bulk flow temperature of the internal flow and the annular flow, respectively.

By substituting equation 4.3 and 4.18 into the energy balance equation, the nodal temperature representing the surface temperature interacting with the internal flow is determined:

$$T_r = \frac{1}{h_i r + \frac{k\left(r + \frac{\Delta r}{2}\right)}{\Delta r}}\left[\frac{k\left(r + \frac{\Delta r}{2}\right)}{\Delta r}T_{r+\frac{\Delta r}{2}} + h_i r T_{b,i}\right]. \tag{4.20}$$

Similarly, by substituting equation 4.4 and 4.20 into the energy balance equation, the nodal temperature representing the surface temperature interacting with the annular flow is determined:

$$T_r = \frac{1}{h_o r + \frac{k\left(r - \frac{\Delta r}{2}\right)}{\Delta r}}\left[h_o r T_{r+\frac{\Delta r}{2}} + \frac{k\left(r - \frac{\Delta r}{2}\right)}{\Delta r}T_{b,i}\right]. \tag{4.21}$$

4.2 Definition of the Model

The size of the control volumes in cylindrical coordinates only varied in the *r*-direction due to the assumed uniform heat distribution in the stator. Due to this, values implying any influence in the axial or azimuthal directions canceled out in all the nodal temperature relationships derived in the preceding sections.

Using a value of 0.01 inches as Δr, the motor section was broken into smaller control volumes which defined the surfaces interacting with the internal and annular flows and the interface surfaces between the different layers within the motor.

The nodal temperature equations were implemented in the model in the following fashion. Equations 4.6, 4.13, and 4.16 defined the nodal temperatures within the motor section components and their interfaces. Equations 4.14 and 4.17 defined the outer radial and inner radial surface control volumes of stator. Equations 4.20 and 4.21 defined the internal and annular flow surface temperature boundaries which were exposed to the key boundary conditions, which in this model were the bulk flow temperatures determined in Section 2.2.1.1. A summary of all nodal relationships pertaining to this analysis is found in Appendix C

The values for the heat transfer coefficients were determined in Section 2.1.3 for a flow rate of 40 ft/s and maximum heat flux:

$$h_i = 180.64 \, W/m^2 K$$

$$h_o = 118.14 \, W/m^2 K .$$

The model was created using Microsoft Excel as a means for creating an analysis within a user-friendly medium for the design engineers. Iterations were conducted until

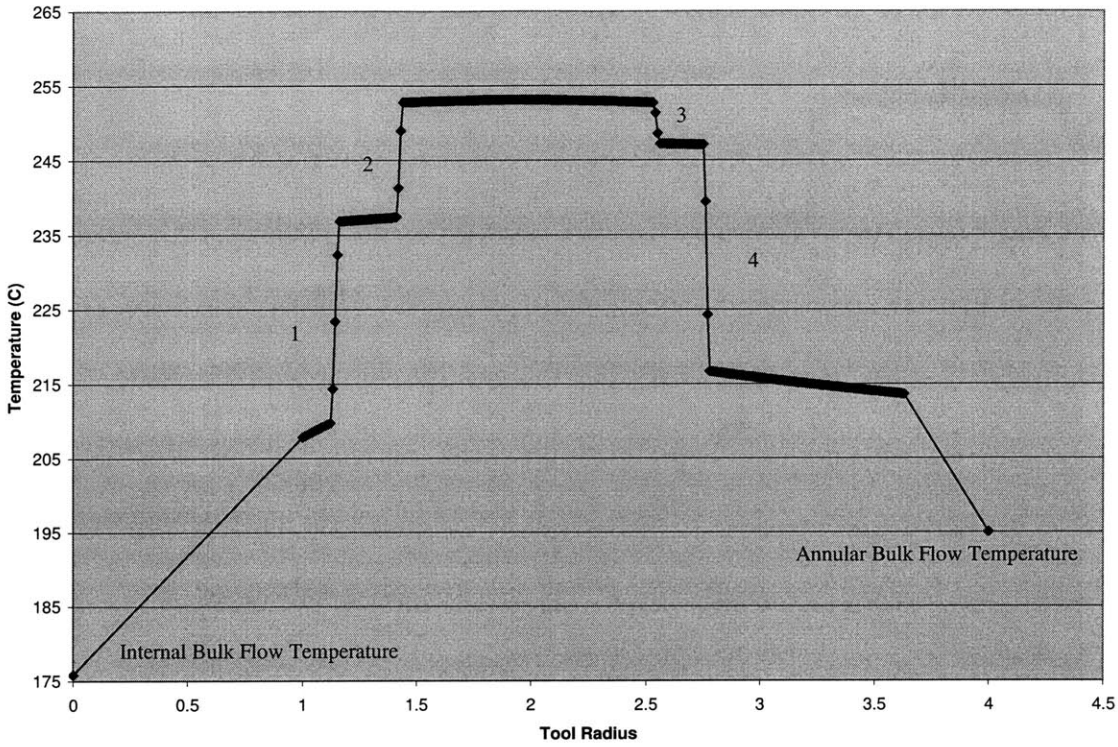

Figure 4.3. Temperature Distribution of Motor Section from Finite Difference Analysis

the maximum change between the nodal temperatures was reduced to the 0.0001 order of magnitude.

In order to validate the model and its nodal relationships, a simplified version of conduction through a concentric annulus was developed using the same equations. This version consisted of a smaller number of control volumes and interface interactions.

4.3 Results

Figure 4.3 shows the results from the finite difference analysis utilizing Excel. The interfaces are defined are shown where the temperature differentials are very high. Section 1 and 2 in Figure 4.3 represents the layer of oil surrounding the rotor shaft. Section 3 represents the epoxy layer that attaches the motor housing to the stator. Section

4 represents the air gap between the drill collar and the motor housing. Because the thermal conductivities of these sections are very low, the heat transfer is not very efficient in these sections.

The key feature of this plot is the distribution of heat in the stator of the motor as shown in Figure 4.4. The plot shows a second order temperature distribution with the maximum temperature occurring at 253.09°C at a radius of 1.93 inches, which tends towards the internal side. However, since the total temperature differential from the minimum temperature to the maximum only spans approximately 0.31 degrees Celsius, the distribution is modeled rather uniformly in the radial direction with respect to the entire distribution in the motor section.

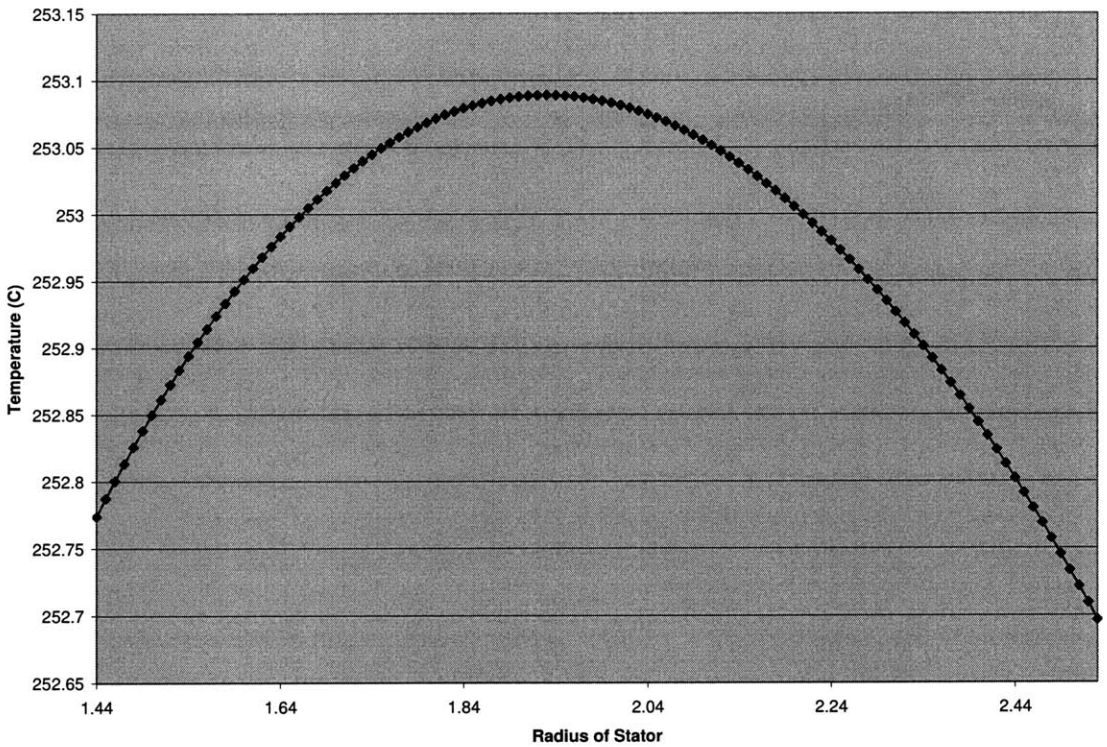

Figure 4.4. Temperature Distribution in Stator from Finite Difference Analysis

At this flow rate, the temperatures within the motor section seem to be very high. Depending on the limits of the electronic components attached to the motor, this heat build up may cause problems that may lead to a system failure. If the thermal conductivities of sections 1 though 4 represented on the graph increased, the heat dissipation in the motor section can be greatly improved.

4.4 Theoretical Temperature Distribution in the Stator

In order to obtain a theoretical temperature distribution of the stator to determine the accuracy of the finite difference analysis, a reduced form of the Laplacian principle in cylindrical coordinates was applied:

$$\frac{1}{r}\frac{\partial}{\partial r}\left(r\frac{\partial T}{\partial r}\right)=-\frac{\dot{q}_v}{k}. \tag{4.22}$$

The θ- and z- components are eliminated because this model assumes no temperature change in those directions.

After one integration, a relationship for the radial temperature gradient is determined:

$$\frac{\partial T}{\partial r}=-\frac{\dot{q}_v}{2k}r^2+c_1\frac{1}{r} \tag{4.23}$$

where c_1 is an integration constant.

By integrating once more, a relationship for the temperature in terms of the radius is obtained:

$$T=-\frac{\dot{q}_v}{4k}r^2+c_1\ln(r)+c_0 \tag{4.24}$$

where c_0 is another integration constant.

In order to determine the integration constants, two conditions can be used. For c_1, a relationship for the total energy in terms of Fourier's law of conduction is used:

$$Q_{m,tot} = -k\frac{\partial T}{\partial r}\bigg|_{r_i} 2\pi r_i L_{motor} - k\frac{\partial T}{\partial r}\bigg|_{r_o} 2\pi r_o L_{motor} \tag{4.25}$$

By substituting equation 4.23 evaluated at r_i and r_o into 4.25, an expression for c_1 is found to be the following:

$$c_1 = \frac{1}{2}\left[\left(\frac{\dot{q}_v}{2k}\right)\left(r_o^2 + r_i^2\right) - \frac{Q_{m,tot}}{2\pi L_{motor} k}\right] \tag{4.26}$$

For c_0, the following equality between Fourier's law of conduction and the heat flux due to change in temperature over the total resistivity is used:

$$-k\frac{\partial T}{dr}\bigg|_k = \frac{1}{2\pi r_k L_{motor}}\frac{T_{s,k} - T_{b,k}}{R_k} \tag{4.27}$$

where *k* represents the evaluation of the terms at either the inner radius or the outer radius of the stator. Since c_1 has already been determined, either boundary can be used. For the bulk flow temperatures, the values determined during the mud flow temperature gradient from Section 2.2.1.1 is used. By solving equation 4.27 for $T_{s,k}$ and equating to equation 4.24 evaluated at boundary *k*, the expression for c_0 is determined to be the following:

$$c_0 = T_{b,k} + \dot{q}_v r_k^2\left(\pi L_{motor} R_k + \frac{1}{4k}\right) - \left[\ln(r_k) + 2\pi L_{motor} R_k k\right]c_1 \tag{4.28}$$

Using these values for the integration constants, the temperature gradient across the radius of the stator was determined as shown in Figure 4.5.

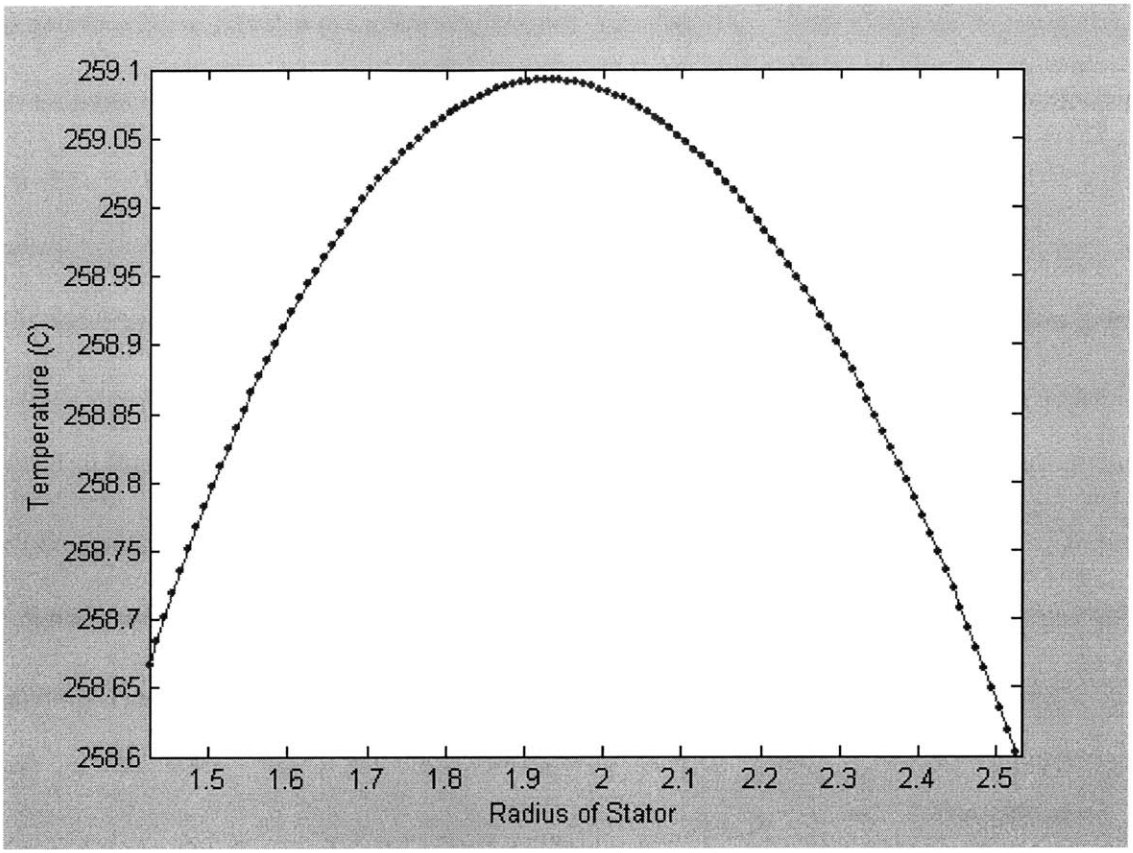

Figure 4.5. Temperature Distribution in Stator from Laplacian Relationship

4.5 Comparison with Cross Section Temperature Distribution

In order to determine the accuracy of the models, the theoretical analysis from section 4.4 was compared with the finite difference analysis and the cross sectional temperature distribution results from Section 2.3.2.

The theoretical result in Figure 4.5 compares well with the result from the finite difference analysis illustrated in Figure 4.4. The maximum temperature for the theoretical model occurs at 259.09°C at a radius of 1.92 inches. The temperature differential from the maximum to the minimum temperature is approximately 0.49°C. These values compare well with those from the finite difference analysis. The maximum temperature both occurs at approximately the same radius. The temperature differential

is only 0.18°C higher in the theoretical model and the scale of the temperature is approximately 6°C higher in the theoretical model. This difference can be accounted for by the iteration conditions of Excel. If the finite difference analysis accuracy was set to a higher order of magnitude (greater than 0.0001), these differences may be reduced even further. From these results, it can be concluded that the finite difference analysis gives an accurate model of the temperature distribution in the stator, and hence, in the motor section.

In comparing with the results from the cross sectional temperature distribution shown in Figure 2.13a, the results agree very well. The magnitudes of the temperatures in Figure 2.13a are approximately 5°C higher. This may be accounted for again by the limitations of Excel as an iteration tool. However, aside from this small difference in magnitude, the trends and slopes of the temperature differentials agree very well. The finite difference analysis is useful because it gives the distribution of heat in the stator as well as shown in Figure 4.4. With the cross sectional temperature distribution models, that detail is omitted.

The motor section at maximum heat generation and minimum heat dissipation conditions may be a cause for concern for the design engineers. The temperatures within the motor section components reach over 250°C, which could cause meltdowns in the electrical components.

CHAPTER 5

CONCLUSION

In developing a thermal analysis of the Direct675 Counter Rotary Steering System for maximum heat flux, maximum mud flow entry temperature, and minimum flow rate conditions, several conclusions on the tool and the analysis were reached.

Results from the thermal analysis of the steering section showed that the exit temperature of the drilling mud flow in the adiabatic bore hole model to be 197.83°C. In the constant environmental heat flux model, the exit temperature was found to be 202.05°C. This small difference of 4.22°C in the exit temperature of the two models implies that the heat flux generated from the bore walls do not have a significant effect on the total heat dissipation effects of the mud flow. This is also evident by recognizing the insignificant difference in the cross sectional temperature distributions of the motor shown in Figure 2.13a and 3.3a and the thrust ring section as shown in Figure 2.13b and 3.3b. The total energy of the bore hole that affects the steering section is relatively low in comparison to the internally generated heat. Therefore, in modeling the steering section, the effects of the environmental heat flux can be considered negligible on the overall thermal analysis of the tool. However, in modeling the drilling mud flow, the environmental factors will influence how the intermediate section dissipates and/or absorbs the energy.

Figure 3.4a, 3.4b, 3.5a, and 3.5b show that an increase in the flow rate or a decrease in the entry temperature of the drilling mud flow can significantly improve its heat absorption properties. The operator of the tool must attempt to optimize these parameters during operation for they are the only controllable parameters that can help the dissipation of heat during operation.

The finite difference analysis of the motor section showed that the stator of the motor reached a maximum temperature of 253.09°C which was in agreement with the maximum temperature obtained from the cross sectional temperature distribution model, which was defined to be approximately 258°C. However, the latter model lacked the detail in the temperature distribution in the stator.

The finite difference analysis determined that the surface temperatures of the stator were 252.77°C on the inner diameter and 252.70°C on the outer radius. This small temperature differential across the radius of the stator implies that it distributes the energy equally to both the inner and outer radius, which is in agreement with the initial assumption.

The accuracy and the reliability of the finite difference analysis were tested with the theoretical model of the stator using Laplacian principles. This theoretical analysis showed that the finite difference analysis gave an accurate assessment of the heat distribution in the stator. The margin of difference could be decrease if the magnitude of accuracy of the iterative process of Excel is increase, or if a stronger iterative tool is utilized.

In terms of the components that make up the motor assembly, heat dissipation can be improved at the layers of the oil which lubricates the rotor shaft, the epoxy layer

which holds the motor housing to the stator, and the air gap between the drilling collar and motor housing. The analysis shows the largest temperature differentials occur in these areas as illustrated in Figure 4.3, the largest being in the first oil layer where the differential is 27.12°C and the air gap where the differential is 30.40°C. If improvements to the thermal conductivities of these layers are made, heat dissipation in the motor section may be improved dramatically, reducing the temperatures that may cause electrical breakdowns.

With the use of both the thermal analysis of the drilling mud and the finite difference analysis, dangerous "hot spots" in the Direct675 counter rotary steerable drilling system were identified. The designers should specifically focus on the motor section due to its electrical components and its predicted high temperatures near the stator at low flow rates. The high temperature of approximately 250°C can very likely cause system failures.

5.1 Modeling Considerations

There are several points to recognize when utilizing the models created in this analysis. One key point is that the models do not take into account the heat dissipated by the actual drilling interface between the bit and the drilling surface. Although the drilling mud acts as a coolant for the tool itself, it also acts as the lubricant and coolant for the drill bit-drilling surface interface. This generates a large amount of heat that can change the nature of the mud flow for the annular flow. This mud also washes away debris created from the drilling which can also affect the flow.

The substitution for the non-Newtonian drilling mud with water will also have an effect on the analysis. Although utilizing the properties of water will give results that will serve the purpose of an initial thermal analysis, utilizing the actual properties of the drilling mud will give more accurate results. However, a conclusion can be made that the properties of water will give reliable results for the purposes giving design engineers an idea of possible problem areas in the oilfield service tool.

5.2 Generalization of Model

In designing oilfield service tools, thermal considerations are often isolated to situations involving electronics because the adverse effects on the system is very obvious. In mechanical design, the effects are not as obvious and often, they are not realized until the tools are designed, prototyped and tested. With a preliminary analysis such as the one described in this paper, such set-backs due to poor heat dissipation can be prevented.

This analysis utilized familiar and user-friendly mediums such as MATLAB and Excel in order to facilitate its application for other oilfield service tools. Using the thermal analysis of the drilling mud and the finite difference analysis, design engineers should be able to create similar models for different tools that serve different functions in order to obtain an understanding on the thermal state of the tool in high heat flux environments. By making relatively simple modifications in the model such as tool dimensions, material properties and heat flux magnitudes, similar models can be created and "hot spots" can be identified.

REFERENCES

[1] Downton, Geoff, Andy Hendricks, Trond Skei Klausen, and Demos Pafitis. "New Directions in Rotary Steerable Drilling." SLB Oilfield Review. Spring 2000, v12, #1. pp. 18-29.

[2] Biggs N., J. Grindrod, C.D. Rayton, C. Sim, and P. Taylor. "Directional technology, steerable systems advance." Drilling Contractor. Jan/Feb 2002, pp. 18-20.

[3] Pafitis, Demos, and Stuart Schaaf. "Field Application of a Fully Rotating Point-the-bit Rotary Steerable System." 2000 SPE Annual Technical Conference and Exhibition. Dallas, Texas, 1-4 October 2000.

[4] Dawe, Richard A. Modern Petroleum Technology. John Wiley & Sons, LTD. New York, 2000.

[5] Incropera, Frank and David DeWitt. Fundamentals of Heat and Mass Transfer. John Wiley & Sons, LTD. New York, 1996.

[6] Aung, Win, Sadik Kakac, and Ramesh K Shah. Handbook of Single-Phase Convective Heat Transfer. John Wiley & Sons, LTD. New York. 1987.

APPENDIX A.

MOTOR ANALYSIS

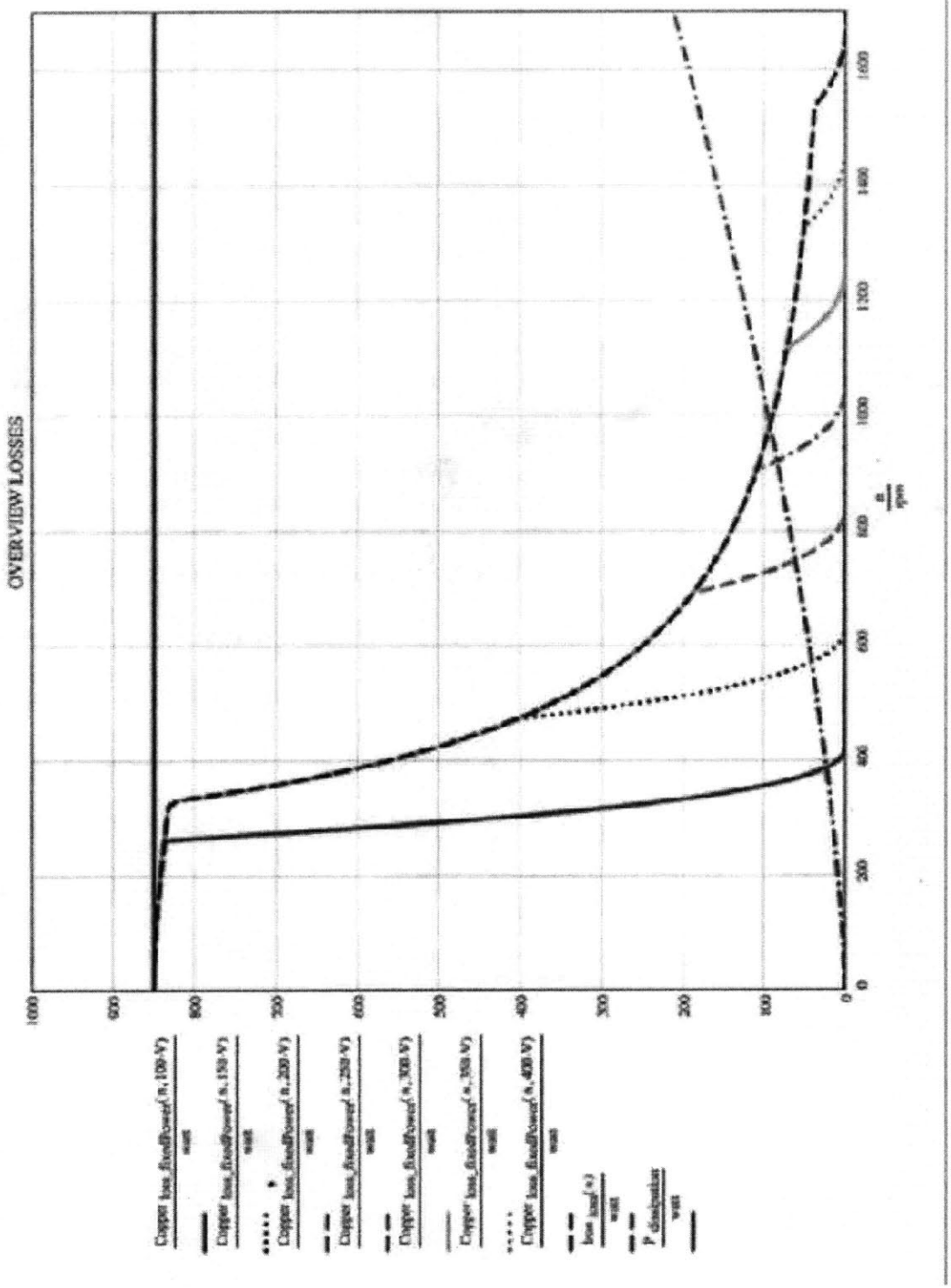

Figure A.1. Overiview Loss of Motor vs. RPM

APPENDIX B.

Resitivities of Subassembly Components

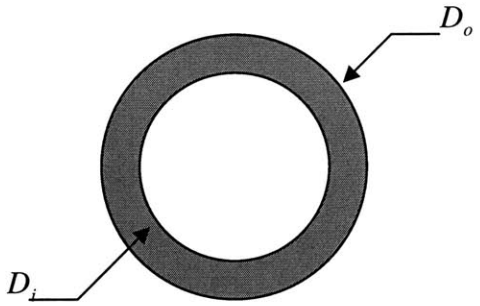

Figure B.1. Resistivity Through a Pipe Wall

In order to determine the resistivity through a component of a tool, the layer is modeled as a pipe wall, and the resistivity is calculated by:

$$R_k = \frac{\ln\left(\frac{r_o}{r_i}\right)}{2\pi k_{th} L} \qquad \text{B.1}$$

where k_{th} is the thermal conductivity of the component k and L is the length of the component k. The radii r_o and r_i are determined by:

$$r_o = \frac{D_o}{2} \qquad \text{B.2}$$

$$r_i = \frac{D_i}{2} \qquad \text{B.3}$$

The total resistivity across several components is determined by:

$$R_{k,tot} = \sum_{1}^{i} R_k \qquad \text{B.4}$$

where i is the number of components in the assembly.

Table B.1 gives the components and their resistivities used to compute the cross sectional temperature distributions for the motor and the thrust ring sections. Table B.2 gives the total resistivities of the intermediate subassemblies as defined in Figure 2.7.

Motor ID	**Resistivity (*K/W*)**
• Flex Tube	0.0082
• Oil Layer 1	0.0945
• Rotor Shaft	0.0021
• Rotor Sleeve	0.000268
• Oil Layer 2	0.0409
Motor OD	
• Epoxy	0.0057
• Motor Housing	0.000334
• Air Gap	0.0226
• Drill Collar	0.0096
Thrust Ring ID	
• Flex Tube	0.0228
• Bit Shaft	0.3551
Thrust Ring OD	
• Bearing Sleeve	0.0054
• Air Gap	0.0287
• Drill Collar	0.0183

Table B.1. Resistivities of Motor and Thrust Ring Section Components

Intermediate Subassembly	**Resistivity (*K/W*)**
• Gear Box	0.1036
• Pressure Compensator	0.8874
• Offset Mandrel	2.3633
• End of Offset Mandrel	2.3289
• Bit Shaft	14.4290

Table B.2. Total Resistivities of Intermediate Subassemblies

APPENDIX C.

SUMMARY OF NODAL TEMPERATURE RELATIONSHIPS

The following equations give the nodal temperature relationships between specified control volumes for a finite difference analysis considering axial and azimuthal symmetry.

CONDUCTION:

$$T_r = \frac{1}{2r}\left[\left(r+\frac{\Delta r}{2}\right)T_{r+\frac{\Delta r}{2}} + \left(r-\frac{\Delta r}{2}\right)T_{r-\frac{\Delta r}{2}}\right] + \frac{\Delta r^2}{2k}\dot{q}_v \qquad \text{C.1}$$

INTERFACE CONDUCTION

Control volume of layer 1 (inner layer):

$$T_r = \frac{1}{\dfrac{k_2}{\ln\left(\dfrac{r_*^{\,k_2-k_1}r_2^{\,k_1}}{r_1^{\,k_2}}\right)} + \dfrac{\left(r_1-\dfrac{\Delta r}{2}\right)}{\Delta r}}\left[\frac{k_2}{\ln\left(\dfrac{r_*^{\,k_2-k_1}r_2^{\,k_1}}{r_1^{\,k_2}}\right)}T_{r+\frac{\Delta r}{2}} + \frac{\left(r_1-\dfrac{\Delta r}{2}\right)}{\Delta r}T_{r-\frac{\Delta r}{2}}\right] \qquad \text{C.2}$$

with internal heat generation:

$$T_r = \frac{1}{\dfrac{k_1k_2}{\ln\left(\dfrac{r_*^{\,k_2-k_1}r_2^{\,k_1}}{r_1^{\,k_2}}\right)} + \dfrac{k_1\left(r_1-\dfrac{\Delta r}{2}\right)}{\Delta r}}\left[\frac{k_1k_2}{\ln\left(\dfrac{r_*^{\,k_2-k_1}r_2^{\,k_1}}{r_1^{\,k_2}}\right)}T_{r+\frac{\Delta r}{2}} + \frac{k_1\left(r_1-\dfrac{\Delta r}{2}\right)}{\Delta r}T_{r-\frac{\Delta r}{2}} + r\Delta r\dot{q}_v\right] \qquad \text{C.3}$$

where:

$$r_* = \left(r_1+\frac{\Delta r}{2}\right) \qquad \text{C.4}$$

Control volume of layer 2 (outer layer):

$$T_r = \frac{1}{\dfrac{k_1}{\ln\left(\dfrac{r_*^{k_2-k_1} r_2^{k_1}}{r_1^{k_2}}\right)} + \dfrac{\left(r_2 + \dfrac{\Delta r}{2}\right)}{\Delta r}} \left[\frac{\left(r_2 + \frac{\Delta r}{2}\right)}{\Delta r} T_{r+\frac{\Delta r}{2}} + \frac{k_1}{\ln\left(\dfrac{r_*^{k_2-k_1} r_2^{k_1}}{r_1^{k_2}}\right)} T_{r-\frac{\Delta r}{2}} \right] \qquad \text{C.5}$$

with internal heat generation:

$$T_r = \frac{1}{\dfrac{k_1 k_2}{\ln\left(\dfrac{r_*^{k_2-k_1} r_2^{k_1}}{r_1^{k_2}}\right)} + \dfrac{k_2\left(r_2 + \dfrac{\Delta r}{2}\right)}{\Delta r}} \left[\frac{k_2\left(r_2 + \frac{\Delta r}{2}\right)}{\Delta r} T_{r+\frac{\Delta r}{2}} + \frac{k_1 k_2}{\ln\left(\dfrac{r_*^{k_2-k_1} r_2^{k_1}}{r_1^{k_2}}\right)} T_{r-\frac{\Delta r}{2}} + r\Delta r \dot{q}_v \right] \qquad \text{C.6}$$

where:

$$r_* = \left(r_2 - \frac{\Delta r}{2}\right) \qquad \text{C.7}$$

<u>CONVECTION</u>

Internal Flow:

$$T_r = \frac{1}{h_i r + \dfrac{k\left(r + \frac{\Delta r}{2}\right)}{\Delta r}} \left[\frac{k\left(r + \frac{\Delta r}{2}\right)}{\Delta r} T_{r+\frac{\Delta r}{2}} + h_i r T_{b,i} \right] \qquad \text{C.8}$$

Annular Flow:

$$T_r = \frac{1}{h_o r + \dfrac{k\left(r - \frac{\Delta r}{2}\right)}{\Delta r}} \left[h_o r T_{r+\frac{\Delta r}{2}} + \frac{k\left(r - \frac{\Delta r}{2}\right)}{\Delta r} T_{b,i} \right] \qquad \text{C.9}$$